

On Learning the Invisible in Photoacoustic Tomography with Flat Directionally Sensitive Detector*

Bolin Pan[†] and Marta M. Betcke[‡]

Abstract. In photoacoustic tomography (PAT) with flat sensor, we routinely encounter two types of limited data. The first is due to using a finite sensor and is especially perceptible if the region of interest is large relatively to the sensor or located farther away from the sensor. In this paper, we focus on the second type caused by a varying sensitivity of the sensor to the incoming wavefront direction which can be modelled as binary *i.e.* by a cone of sensitivity. Such visibility conditions result, in Fourier domain, in a restriction of both the image and the data to a bowtie, akin to the one corresponding to the range of the forward operator. The visible ranges, in image and data domains, are related by the wavefront direction mapping. We adapt the wedge restricted Curvelet decomposition, we previously proposed for the representation of the full PAT data, to separate the visible and invisible wavefronts in the image. We optimally combine fast approximate operators with tailored deep neural network architectures into efficient learned reconstruction methods which perform reconstruction of the visible coefficients and the invisible coefficients are learned from a training set of similar data.

Key words. learned image reconstruction, compressed sensing, Curvelet transform, photoacoustic tomography, fast Fourier methods, limited view

AMS subject classifications. 94A08, 97R40, 94A12, 92C55, 65T50, 68U10

1. Introduction. Photoacoustic Tomography (PAT) is a hybrid imaging modality that can deliver high resolution *in-vivo* images of absorbed optical energy upon illumination with laser-generated near infra-red light pulse [59, 11, 44, 57, 65, 60]. PAT harnesses the photoacoustic effect to encode optical contrast onto broadband ultrasonic waves thereby circumventing the depth and spatial resolution limitations of purely optical imaging techniques.

If the data is measured over a surface surrounding the region of interest for long enough time and using omnidirectional sensors, the reconstruction can be obtained via *time reversal* which amounts to a single solve of a wave equation; see section 2 for details. In practice, the limited-view problems are introduced due to spatially and/or directionally restricted sampling of the ultrasound (US) waves. An example of the former is a finite size linear/planar sensor placed on one side of the domain, and of the latter most US sensors' incapability of recording wavefronts impinging on the detector at angles beyond $\pm\theta_{\max}$, $\theta_{\max} < \pi/2$. Another type of limited-view problems result from restricting the length of the recorded time series, a necessity arising in a case of trapping sound speeds. As in this work we focus on constant speed of sound, we do not consider this last type of limited-view problems.

For limited-data problems due to sparse sampling rather than limited-view, compressed sensing (CS) approaches that iteratively minimise a penalty function combining an explicit model of US propagation with constraints on the image as regularisation [38, 10, 8, 33, 39, 15,

*Submitted to the editors April 16, 2022.

Funding: M. Betcke would like to acknowledge support from EPSRC EP/T014369/1, EP/W007673/1.

[†]Department of Computer Science, University College London, UK (bolin.pan.15@ucl.ac.uk).

[‡]Department of Computer Science, University College London, UK (m.betcke@ucl.ac.uk)

[52, 45, 28, 30, 26, 27, 29, 47] have proven to provide significantly better reconstructions than *time reversal* and more general Newton series based iterative methods which lack inherent regularisation. A shared drawback of all these methods is high computational complexity of iterating with the forward and adjoint/inverse operators. This shortcoming has been addressed by two step methods which reconstruct complete data first and then obtain the image through single time reversal [33, 13, 45], which however usually sacrifice some reconstruction quality for efficiency.

For the considered limited-view problems the situation is more dire. Time reversal and Newton series methods as expected only reconstruct the visible singularities producing images with characteristic limited-view artefacts and lack noise suppression properties of CS methods [63]. Performance of compressed sensing depends on the choice of the prior, e.g. while total variation (TV) yields overall better reconstructions than Curvelet sparsity (reasons for which are discussed in subsection 6.3), even for TV the directions of singularities missing from the data result in inherent blur in the reconstructed images.

A decade after the breakthrough in Deep Neural Networks, Deep Learning (DL) techniques are ubiquitous in tomographic imaging [41, 40, 34, 1, 66, 2, 9]. In comparison to CS, the learned approaches i) need fewer applications of the forward/adjoint operator which leads to more efficient reconstruction algorithms, ii) have the ability to extract prior information about the image from a training set of similar images which makes them particularly suitable for e.g. medical image reconstruction where patient studies fit such scenario. DL approaches to PAT image reconstruction mainly fall in one of the two categories: i) learned post-processing of a simple reconstruction such as e.g. pseudo-inverse, ii) learned iterative reconstruction (also referred to as model based learning).

The learned post-processing usually employs a network with many layers and learnable parameters capable of encoding complicated image priors. The learned post-processing of the universal back-projection [61] was studied in [6, 7, 5, 51, 50, 43], of the first iteration of an averaged time reversal in [53] and of time reversal in [32]. All but the last work use standard U-Net architecture, while the last uses a dense U-Net (an U-Net with dense blocks and skip connections). The main advantage of learned post-processing is that an initial simple reconstruction can be decoupled from the iterative training process. This obviously limits the impact of the physical model on the reconstruction procedure and hence makes the process less robust and more dependent on the training set used.

Learned iterative reconstruction approaches are based on unrolling of iterative solvers and parametrising the proximal map with neural networks, usually much smaller than those used in learned post-processing, e.g. [54, 17, 16, 14, 64]. Due to repeated application of the forward and adjoint/approximate inverse operators on the training set, learned iterative reconstruction methods for 3D PAT suffer from unreasonable training times. To tackle this, a greedy training for learned gradient schemes for 3D PAT was suggested in [37]. The same authors later considered use of efficient Fourier domain approximate forward model to accelerate the training process [35], which is also the direction we take in this work.

Other proposed approaches include learned pre-processing of the data prior to reconstruction, fully learned methods completely bypassing the physics of the model, and methods that aim to learn some representation of the regulariser for use in variational framework, we refer to [36] for a review of such approaches specific to PAT.

1.1. Related work. In series of papers Frikel and Quinto [47, 26, 29, 27, 48] characterised the visibility of singularities in X-ray tomography and in [63, 30] in PAT with finite omnidirectional flat sensor ($\theta_{\max} = \pi/2$). The limitations of CS approaches with Curvelet sparsity regularisation were discussed in [26, 27] in the context of X-ray tomography.

Motivated by these works, a number of authors considered implications of the visible and invisible singularities for learning methods in limited-angle tomography in X-ray and in general [19, 18, 3]. In [3] the authors proposed an approach which uses the canonical relation between the singularities of the Radon transform, in image and data domains, to inpaint the singularities extracted from the data using network proposed in [4] into the reconstructed image. In [18] the authors reinterpret the unrolled ISTA iteration as CNN layers which coefficients and structure are inferred from the convolutional properties of Fourier integral operators and pseudo-differential operators and apply it to limited-angle X-ray tomography. The present work is closest in spirit to the approach proposed in [19] for the limited-angle X-ray tomography which promotes the idea to separate the visible part of the image, which can be stably reconstructed in Shearlets frame using CS approach, from the invisible part of the image which needs to be learned. The main benefits of such approach are i) a clear separation between what is reconstructed from the measured data and the prior that is learned from the training set and ii) decoupling of the reconstruction of the visible which requires iterating with the forward/adjoint operator from learning the invisible which does not, as the invisible is contained in the null space of the forward operator. A similar idea was proposed from an algebraic perspective as null space learning in [49].

1.2. Motivation. In this work we focus on the limited-view problem due to varying sensitivity of the sensor to the direction of the wavefront impinging on the detector. The directional sensitivity can be modelled as binary with a maximal impingement angle $\pm\theta_{\max}$, $\theta_{\max} < \pi/2$, for the wavefronts to be registered, resulting in a cone of sensitivity around the direction normal to the sensor. We observe this problem shares many similarities with the limited-angle for parallel X-ray transform, in particular the decomposition into visible/invisible singularities in the Fourier domain which can be strictly realised using directional frames like Curvelets or Shearlets. This decomposition into visible and invisible singularities for limited-angle parallel X-ray geometry underpins the result in [27] on visible singularities only recovery via compressed sensing in Curvelets or Shearlets frames.

Based on this result, the authors of [19] proposed to reconstruct the visible and learn the invisible in Shearlet frame for the limited-angle parallel X-ray tomography. These results along with the above observation of similarities between the limited-angle parallel X-ray CT and limited view (due to sensitivity angle) in flat sensor PAT motivate our work.

Using the wavefront mapping (**WfM**) [45], we obtain the correspondence between the visible and invisible wavefront directions in PAT image and PAT data. This allows us the observation that the limited sensitivity angle restricts the data range in a way that enables use of efficient Fourier domain forward/adjoint and pseudoinverse operators derived in [subsection 3.1](#).

We adapt the wedge restricted Curvelet transform, proposed in [45] for PAT data representation, to the representation of the visible/invisible components of the PAT image (initial pressure, p_0), and recover the visible singularities via CS in a wedge restricted Curvelet frame

with the data fidelity term using the aforementioned limited angle PAT Fourier operators. The visible component of the PAT image is then represented by its Coronae coefficients, a minimal representation which perfectly matches the split into the visible/invisible and the multiscale structure induced by the Curvelet frame, introduced in [subsection 5.2.2](#). These visible Coronae coefficients are fed into a Coronae-Net, a tailored U-Net inspired architecture, designed and trained to fill in the invisible component of the PAT image given the visible component.

2. Photoacoustic Tomography. With several assumptions on the tissue properties [\[58\]](#), the photoacoustic forward problem can be modelled as an initial value problem for the free space wave equation

$$(A) \quad \underbrace{\left(\frac{1}{c^2(\mathbf{x})} \frac{\partial^2}{\partial t^2} - \nabla^2 \right)}_{:=\square^2} p(t, \mathbf{x}) = 0, \quad (t, \mathbf{x}) \in (0, T) \times \mathbb{R}^d,$$

$$p(0, \mathbf{x}) = p_0(\mathbf{x}),$$

$$p_t(0, \mathbf{x}) = 0,$$

where $p(t, \mathbf{x}) \in \mathcal{C}^\infty((0, T) \times \mathbb{R}^d)$ is a time dependent acoustic pressure recorded for a finite time T , $p_0(\mathbf{x}) \in \mathcal{C}_0^\infty(\mathbb{R}^d)$ is its initial value, and $c(\mathbf{x}) \in \mathcal{C}^\infty(\mathbb{R}^d)$ is the speed of sound in the tissue.

The photoacoustic inverse problem recovers the initial pressure $p_0(\mathbf{x})$ in the region of interest Ω on which $p_0(\mathbf{x})$ is compactly supported, from time dependent measurements

$$g(t, \mathbf{x}_S) = \omega(t)p(t, \mathbf{x}_S), \quad (t, \mathbf{x}_S) \in (0, T) \times \mathcal{S}$$

at a set of locations $\mathbf{x}_S \in \mathcal{S} \subset \mathbb{R}^d$, e.g. the boundary of Ω , where $\omega \in \mathcal{C}_0^\infty(0, T)$ is a temporal smooth cut-off function. It amounts to a solution of the following initial value problem for the wave equation with constraints on the surface [\[25\]](#)

$$(TR) \quad \begin{aligned} \square^2 p(t, \mathbf{x}) &= 0, & (t, \mathbf{x}) &\in (0, T) \times \mathbb{R}^d, \\ p(0, \mathbf{x}) &= 0, \quad p_t(0, \mathbf{x}) = 0, \\ p(t, \mathbf{x}) &= g(T - t, \mathbf{x}_S), & (t, \mathbf{x}_S) &\in (0, T) \times \mathcal{S}, \end{aligned}$$

also referred to as a *time reversal*. For non-trapping smooth $c(\mathbf{x})$, in 3D, the solution of [\(TR\)](#) is the solution of the PAT inverse problems if T is chosen large enough so that $g(t, \mathbf{x}) = 0$ for all $\mathbf{x} \in \Omega$, $t \geq T$ and the wave has left the domain Ω . Assuming that the measurement surface \mathcal{S} surrounds the region of interest Ω containing the support of initial pressure p_0 , the wave equation [\(TR\)](#) has a unique solution.

When no complete data is available (meaning that some singularities have not been observed at all as opposed to the case where partial energy has been recorded, see e.g. [\[56\]](#)), p_0 is usually recovered in a variational framework, including some additional penalty functional corresponding to prior knowledge about the solution. Iterative methods for solution of such problems require application of the adjoint operator which amounts to the solution of the

following initial value problem with time varying mass source [10]

$$(A^*) \quad \begin{aligned} \square^2 q(t, \mathbf{x}) &= \begin{cases} \frac{\partial}{\partial t} g(T-t, \mathbf{x}_S), & (t, \mathbf{x}_S) \in (0, T) \times \mathcal{S} \\ 0 & \text{everywhere else} \end{cases} \\ q(0, \mathbf{x}) &= 0, \\ q_t(0, \mathbf{x}) &= 0, \end{aligned}$$

evaluated at T , $q(T, \mathbf{x})$.

3. Fourier domain formulation of PAT. The operators defined in this section map between Fourier transforms of the initial pressure p_0 and the data g . When using Fourier domain PAT operators in conjunction with Curvelet frame (which is also defined and computed via the Fourier transform), all the computations can be carried out directly in Fourier domain without need to compute intermediate Fourier transforms.

3.1. Forward, adjoint and inverse PAT operators in Fourier domain. Assuming half space symmetry as per line sensor geometry in 2D (plane sensor in 3D) with a constant speed of sound $c(\mathbf{x}) = c$, the solution of the wave equation (A) in Fourier domain can be explicitly written as [23]

$$(3.1) \quad \hat{p}(t, \mathbf{k}) = \cos(c|\mathbf{k}|t)\hat{p}_0(\mathbf{k}),$$

where \hat{u} denotes the Fourier transform of u in some or all variables and $\mathbf{k} \in \mathbb{R}^d$ is the Fourier domain wave vector. Using (3.1), we can obtain the following *forward* mapping between the initial pressure $p_0(\mathbf{x}_\perp, \mathbf{x}_S)$, $(\mathbf{x}_\perp, \mathbf{x}_S) \in \mathbb{R} \times \mathbb{R}^{d-1}$ and the PAT data $g(ct, \mathbf{x}_S)$, $(ct, \mathbf{x}_S) \in \mathbb{R} \times \mathbb{R}^{d-1}$ with $g(ct, \mathbf{x}_S) = p(ct, \mathbf{x}_S)$ in Fourier domain [23, 42, 62, 13]

$$(\hat{A}) \quad \hat{g}(\omega/c, \mathbf{k}_S) = \frac{\omega/c}{\sqrt{(\omega/c)^2 - |\mathbf{k}_S|^2}} \hat{p}_0 \left(\sqrt{(\omega/c)^2 - |\mathbf{k}_S|^2}, \mathbf{k}_S \right),$$

where \cdot_\perp denotes the ambient space coordinate perpendicular to the sensor, time t and its frequency ω are understood as non-negative quantities, with symmetries defining the functions on their negatives. In particular, formula (3.1) has an implicit assumption of even symmetry of $p_0(\mathbf{x}_\perp, \mathbf{x}_S)$, $g(ct, \mathbf{x}_S)$ in \mathbb{R}^d w.r.t. $\mathbf{x}_\perp = 0$, $ct = 0$, respectively,

$$(3.2) \quad \begin{aligned} \hat{p}_0(-\mathbf{k}_\perp, \mathbf{k}_S) &= \hat{p}_0(\mathbf{k}_\perp, \mathbf{k}_S), \\ \hat{g}(-\omega/c, \mathbf{k}_S) &= \hat{g}(\omega/c, \mathbf{k}_S). \end{aligned}$$

The constant speed of sound c is used to normalise time/frequencies, the non-normalised formulation contains additional factor $1/c$ on the right hand side of (A) [45]. For the right hand side of equation (A) to be real and bounded, the expression under the square root should be bounded away from zero for all non-zero wave vectors *i.e.* $\mathcal{R}_A = \{(\omega/c, \mathbf{k}_S) \in \mathbb{R}^d : |\mathbf{k}_S| < \omega/c\} \cup \mathbf{0}$, resulting in a bow-tie shaped range of photoacoustic operator in the sound-speed normalised Fourier space, see Figure 2 (b). We note that (A) turned around underlies the inverse transform (which is stable) [42], but as forward transform the factor blows up and regularisation is required [35].

As already alluded, the inverse PAT Fourier operator follows immediately from $(\hat{\mathbf{A}})$,

$$(\hat{\mathbf{A}}^{-1}) \quad \hat{p}_0(\mathbf{k}_\perp, \mathbf{k}_S) = \frac{|\mathbf{k}_\perp|}{|\mathbf{k}|} \hat{g}(|\mathbf{k}|, \mathbf{k}_S),$$

with the change of variables induced by the dispersion relation in the wave equation $(\omega/c)^2 = |\mathbf{k}|^2 = |\mathbf{k}_S|^2 + |\mathbf{k}_\perp|^2$,

$$(3.3) \quad \begin{aligned} \mathbf{k} = (\mathbf{k}_\perp, \mathbf{k}_S) &\leftarrow \left(\sqrt{(\omega/c)^2 - |\mathbf{k}_S|^2}, \mathbf{k}_S \right), \\ (\omega/c, \mathbf{k}_S) &\leftarrow \left(|\mathbf{k}| = \sqrt{|\mathbf{k}_\perp|^2 + |\mathbf{k}_S|^2}, \mathbf{k}_S \right). \end{aligned}$$

Using the definition the adjoint, the adjoint PAT Fourier operator was derived in the Appendix A

$$(\hat{\mathbf{A}}^*) \quad \hat{p}_0(\mathbf{k}_\perp, \mathbf{k}_S) = \hat{g}(|\mathbf{k}|, \mathbf{k}_S).$$

We note that both inverse $(\hat{\mathbf{A}}^{-1})$ and adjoint $(\hat{\mathbf{A}}^*)$ operators only differ by the scaling factor present in the inverse and absent from the adjoint, while the underlying change of variables is the same.

3.2. Wavefront direction mapping. The wave front mapping (**WfM**) was derived in [45] observing that the change of coordinates (3.3) defines a one-to-one map between the frequency vectors $\mathbf{k} = (\mathbf{k}_\perp, \mathbf{k}_S) \in \mathbb{R}^d$ and $(\omega/c, \mathbf{k}_S) \in \mathcal{R}_{\mathbf{A}}$. This mapping is illustrated below. Figure 1 (a) shows the wavefronts and the corresponding wavefront vectors in the ambient space $\bar{\theta} = (-\cos \theta, \sin \theta)$ on the left and in the data space $\bar{\beta} = (\cos \beta, -\sin \beta)$ on the right. Note, that these wavefront vectors have the same direction as their frequency domain counterparts $\mathbf{k}_{\bar{\theta}}, \mathbf{k}_{\bar{\beta}}$ which are depicted in Figure 1 (b). The even symmetry (3.2) is inherited by the map (3.3).

With the notation in Figure 1, we deduce the map between the wavefront vector angles $\bar{\theta}$ and $\bar{\beta}$ (which are the same in space and frequency domains)

$$(3.4) \quad \tan \bar{\beta} = \frac{\mathbf{k}_S^{\bar{\beta}}}{\mathbf{k}_{\omega/c}^{\bar{\beta}}} = \frac{-\mathbf{k}_S^{\bar{\theta}}}{|\mathbf{k}_{\bar{\theta}}|} = \frac{-\mathbf{k}_S^{\bar{\theta}}}{\sqrt{(|\mathbf{k}_\perp^{\bar{\theta}}|^2 + |\mathbf{k}_S^{\bar{\theta}}|^2)}} = \sin(-\bar{\theta}).$$

Using the relation with wavefront vector angles $\bar{\theta} = \pi - \theta, \bar{\beta} = 2\pi - \beta$ and basic trigonometric identities, from equation (3.4), we obtain the corresponding map between θ and β

$$(\mathbf{WfM}) \quad \beta = \arctan(\sin \theta),$$

where $\theta \in (-\pi/2, \pi/2)$ and $\beta \in (-\pi/4, \pi/4)$ for the un-mirrored initial pressure. The derivation was presented in $\mathbb{R}^d, d = 2$ for simplicity, $d = 3$ follows analogously by treating both detector coordinates the same, see also [45].

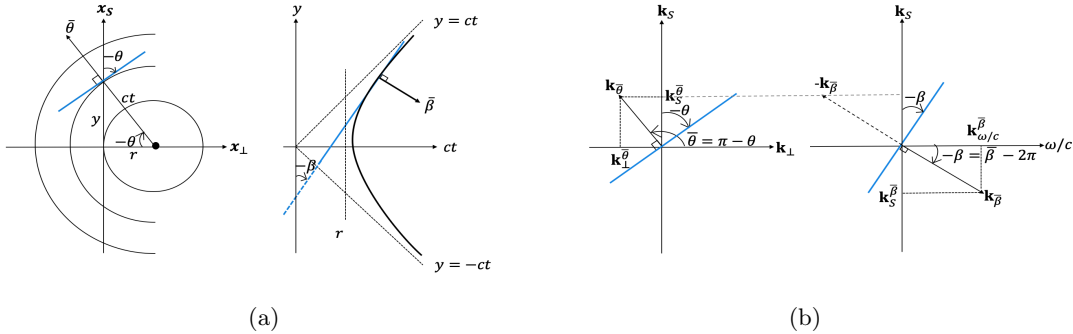


Figure 1: (a) Wavefront direction mapping between the ambient space $\bar{\theta}$ (left), and the data space, $\bar{\beta}$ (right) on an example of a 2D spherical wave. $-\theta$ and $-\beta$ are the angles that the wavefronts (in blue) make with the sensor plane. (b) The Fourier domain counterpart, the wavefront vector mapping between $\mathbf{k}_{\bar{\theta}}$ (left), and $\mathbf{k}_{\bar{\beta}}$ (right).

3.3. Limited-angle PAT Fourier operators. According to the wavefront mapping (**WfM**) we have

$$\tan \beta_{\max} = \sin \theta_{\max},$$

which yields the correspondence between the visible ambient space wavefronts $[-\theta_{\max}, \theta_{\max}]$, $\theta_{\max} < \pi/2$ and the visible data space wavefronts $\beta \in [-\beta_{\max}, \beta_{\max}]$, $\beta_{\max} < \pi/4$. Thus we only need to restrict the range of θ in equation $(\hat{\mathbf{A}})$ to formulate the limited-angle PAT Fourier forward operator

$$(\hat{\mathbf{A}}_{\angle}) \quad \hat{g}(\omega/c, \mathbf{k}_S) = \frac{\omega/c}{\sqrt{(\omega/c)^2 - |\mathbf{k}_S|^2}} \hat{p}_0 \left(\sqrt{(\omega/c)^2 - |\mathbf{k}_S|^2}, \mathbf{k}_S \right), \quad |\mathbf{k}_S| \leq \sin(\theta_{\max}) |\mathbf{k}|.$$

$(\hat{\mathbf{A}}_{\angle})$ maps from the domain $\mathcal{D}_{\mathbf{A}}^{\angle} = \{(\mathbf{k}_\perp, \mathbf{k}_S) \in \mathbb{R}^d : |\mathbf{k}_S| \leq \sin(\theta_{\max}) |\mathbf{k}| \}$, $\sin \theta_{\max} < 1$ onto the narrowed bow-tie shaped range $\mathcal{R}_{\mathbf{A}}^{\angle} = \{(\omega/c, \mathbf{k}_S) \in \mathbb{R}^d : |\mathbf{k}_S| \leq (\omega/c) \tan \beta_{\max} \}$, $\tan \beta_{\max} < 1$.

A Fourier domain illustration of the visibility in ambient space for $\theta_{\max} = \pi/3$ is shown in Figure 2 (a), and the corresponding narrowing down of the bow-tie shaped range in Fourier transformed data space is highlighted with the red cut-off line in Figure 2 (b). With this restriction $|\theta| \leq \theta_{\max} < \pi/2$, the denominator of $(\hat{\mathbf{A}}_{\angle})$ is bounded away from 0,

$$(3.5) \quad (\omega/c)^2 - |\mathbf{k}_S|^2 \geq (1 - \tan^2 \beta_{\max}) (\omega/c)^2 = (\omega/c)^2 \cos^2 \theta_{\max} > 0,$$

and the limited-angle PAT Fourier forward operator can be stably evaluated. We note, that our restriction is equivalent to an upper bound on the factor (suggested as regularisation in [35])

$$(3.6) \quad \frac{\omega/c}{\sqrt{(\omega/c)^2 - |\mathbf{k}_S|^2}} = \frac{|\mathbf{k}|}{|\mathbf{k}_\perp|} = \frac{1}{\cos \theta} \leq D,$$

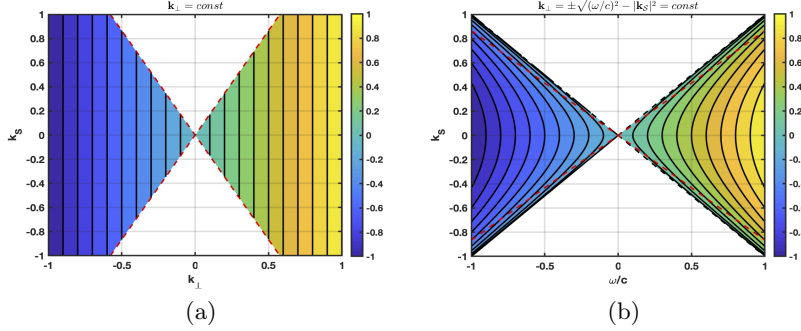


Figure 2: Contour plot of $\mathbf{k}_\perp = \text{const}$ over the bow-tie shaped (a) domain of the limited angle PAT Fourier forward operator, $\theta_{\max} = \pi/3$, (b) range of the PAT Fourier forward operator with the further narrowed range of the limited angle PAT Fourier forward operator highlighted with the red dashed line.

with the choice of $D = (\cos \theta_{\max})^{-1}$.

We can now analogously define the limited-angle PAT Fourier inverse operator, $\mathcal{R}_A^\angle \rightarrow \mathcal{D}_A^\angle$

$$(\hat{\mathbf{A}}_\angle^{-1}) \quad \hat{p}_0(\mathbf{k}_\perp, \mathbf{k}_S) = \frac{|\mathbf{k}_\perp|}{|\mathbf{k}|} \hat{g}(|\mathbf{k}|, \mathbf{k}_S), \quad |\mathbf{k}_S| \leq \sin(\theta_{\max})|\mathbf{k}|,$$

and the limited-angle PAT Fourier adjoint operator, $\mathcal{R}_A^\angle \rightarrow \mathcal{D}_A^\angle$

$$(\hat{\mathbf{A}}_\angle^*) \quad \hat{p}_0(\mathbf{k}_\perp, \mathbf{k}_S) = \hat{g}(|\mathbf{k}|, \mathbf{k}_S), \quad |\mathbf{k}_S| \leq \sin(\theta_{\max})|\mathbf{k}|.$$

We note, that in practice the functions p_0, g are discretized on a grid in \mathbb{R}^d and discrete fast Fourier transforms along with interpolation are used for evaluation of the operators. We use the same notation for the continuous and discrete operators, as their meaning is clear from the context.

Finally, we consider a non-variational approach based on the Neumann-series [56, 46] which is known to effectively restore partially visible singularities which arise in limited-view problems. The k -th iterate in the Neumann series approach with the limited-angle PAT Fourier operators is obtained as

$$(\text{iN}) \quad p_{\text{iN}}^k = \sum_{i=0}^k K^i \hat{\mathbf{A}}_\angle^{-1} g_\angle, \quad \text{with} \quad K = I - \hat{\mathbf{A}}_\angle^{-1} \hat{\mathbf{A}}_\angle,$$

where I is the identity operator over \mathbb{R}^d and $g_\angle = \hat{\mathbf{A}}_\angle p_0$ is the limited-angle data (here

noiseless). The reformulation of **(iN)** leads to an iterative image reconstruction scheme

$$\begin{aligned} p_{\mathbf{iN}}^{k+1} &= \sum_{i=0}^{k+1} K^i \hat{\mathbf{A}}_{\angle}^{-1} g_{\angle} = K \sum_{i=0}^k K^i \hat{\mathbf{A}}_{\angle}^{-1} g_{\angle} + \hat{\mathbf{A}}_{\angle}^{-1} g_{\angle} = K p_{\mathbf{iN}}^k + \hat{\mathbf{A}}_{\angle}^{-1} g_{\angle} \\ &= (I - \hat{\mathbf{A}}_{\angle}^{-1} \hat{\mathbf{A}}_{\angle}) p_{\mathbf{iN}}^k + \hat{\mathbf{A}}_{\angle}^{-1} g_{\angle} \\ &= p_{\mathbf{iN}}^k - \hat{\mathbf{A}}_{\angle}^{-1} (\hat{\mathbf{A}}_{\angle} p_{\mathbf{iN}}^k - g_{\angle}). \end{aligned}$$

The effect of the limited-angle PAT Fourier forward model in data domain is demonstrated in **Figure 3** on the 4-disk phantom with line sensor on top. The disks are placed inside the north sector of the square domain so to eliminate any effect of the finite sensor. Comparing the approximated full-angle data ($\theta_{\max} \approx \pi/2$) in (b) with the limited-angle data ($\theta_{\max} = \pi/4$)¹ in (c), we observe Gibbs like phenomena, i.e. the aliasing is more perceptible for a larger range of visible angles leading to a larger sup norm. On the first sight, there is an apparent similarity between (d) the limited-angle inversion $p_0^{\text{Linear}} = \hat{\mathbf{A}}_{\angle}^{-1} g_{\angle}$ and (e) the limited-angle adjoint $p_0^{\text{Adj}} = \hat{\mathbf{A}}_{\angle}^* g_{\angle}$, however we point out a noticeable difference in contrast due to the frequency dependent factor $|\mathbf{k}|/|\mathbf{k}_{\perp}|$ present in the inverse but not in the adjoint. We observe that the Neumann series reconstruction **iN**(g_{\angle}) (f) is almost the same as the direct linear inversion p_0^{Linear} (d). This is a consequence of the half space geometry with planar / line sensor, where each wavefront is measured exactly once, i.e. we measure the wavefront travelling towards the detector and the wavefront in the opposite direction is accounted for by assuming the mirror symmetry of the data w.r.t. the detector hyperplane. Thus the limited angle (nor actually the limited sensor) does not result in any partially measured singularities (all or nothing) and hence no improvement can be expected by the iterative Neumann series approach.

4. Multiscale Representation of Photoacoustic Initial Pressure.

4.1. Curvelets. Curvelet transform [20] is a multiscale pyramid with many directions and positions at each scale. **Figure 4** (a) shows the Curvelet induced tiling of the Fourier domain in 2D, with Curvelet window functions supported near a trapezoidal wedge with the orientation θ_l , $\theta_l \in [-\pi, \pi)$ and the scale j . The corresponding Curvelet envelope function in spatial domain is aligned along a ridge of length $2^{-j/2}$ and width 2^{-j} . The wedges/envelopes become finer with increasing scale which lends the Curvelet frame the ability to resolve singularities along curves.

We introduce the Curvelet transform following the continuous presentation in [20]. For each scale j , orientation $\theta_l = 2\pi/L \cdot 2^{-\lfloor j/2 \rfloor} \cdot l$, $l \in \mathbb{Z}^{d-1}$ such that $\theta_l \in [-\pi, \pi)^{d-1}$ ($L \cdot 2^{\lfloor j_0/2 \rfloor}$ is the number of angles at the second coarsest scale $j = j_0 + 1$, j_0 even), and translation $\mathbf{a} \in \mathbb{Z}^d$, the Curvelet coefficients of $u : \mathbb{R}^d \rightarrow \mathbb{R}$, are computed as

$$(C) \quad C_{j,l}(\mathbf{a}) = \int_{\mathbb{R}^d} \hat{u}(\mathbf{k}) \tilde{U}_{j,\theta_l}(\mathbf{k}) e^{i\mathbf{x}_{\mathbf{a}}^{(j,l)} \cdot \mathbf{k}} d\mathbf{k},$$

which is a projection of the Fourier transform $\hat{u}(\mathbf{k})$ on the corresponding frame element function $\tilde{U}_{j,\theta_l}(\mathbf{k}) \exp(-i\mathbf{k} \cdot \mathbf{x}_{\mathbf{a}}^{(j,l)})$ with $\tilde{U}_{j,\theta_l}(\mathbf{k})$ a trapezoidal frequency window with scale j and

¹In real data acquisition scenarios with Fabry Perròt sensor, θ_{\max} is empirically found to be $\approx \pi/4$.

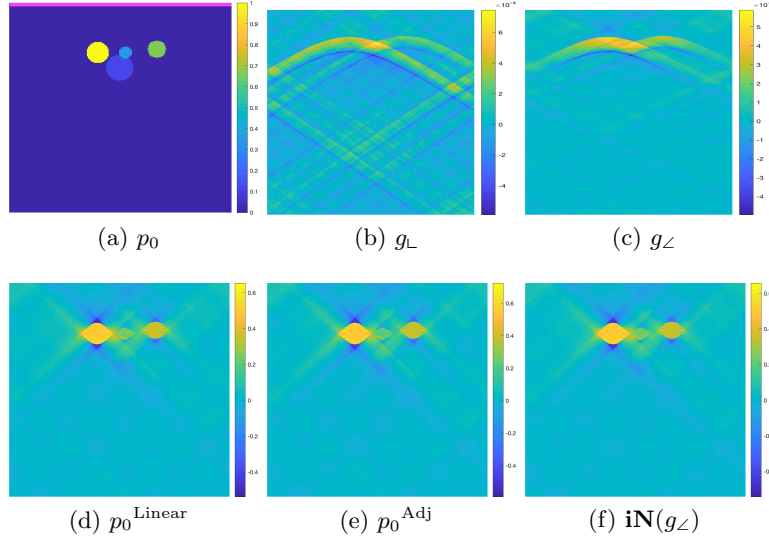


Figure 3: 4-disk Phantom - Limited-angle PAT Fourier operators: (a) p_0 : 4 disks in north sector of a square and a line detector on top (in pink), (b) full-angle data g_L obtained via PAT Fourier forward operator $g_L = \hat{\mathbf{A}}p_0$ (a.k.a $\theta_{\max} \approx \pi/2$) and (c) limited-angle data $g_L = \hat{\mathbf{A}}_L p_0$ with $\theta_{\max} = \pi/4$, (d) direct linear inversion of limited-angle data, $p_0^{\text{Linear}} = \hat{\mathbf{A}}_L^{-1} g_L$, (e) backprojection of g_L , $p_0^{\text{Adj}} = \hat{\mathbf{A}}_L^* g_L$, and (f) Neumann-series reconstruction of g_L after 20 iterations.

orientation θ_l , and a spatial domain centre at $\mathbf{x}_{\mathbf{a}}^{(j,l)}$ corresponding to the sequence of translation parameters $\mathbf{a} = (a_1 \cdot 2^{-j}, a_2 \cdot 2^{-j/2}, \dots, a_d \cdot 2^{-j/2})$, $(a_1, \dots, a_d) \in \mathbb{Z}^d$. Note that the coarse scale Curvelets are isotropic Wavelets corresponding to translations of an isotropic low pass window $\tilde{U}_0(\mathbf{k})$. The window functions at all scales and orientations form a smooth partition of unity on the relevant part of \mathbb{R}^d . For real function u , we use the symmetric version of the Curvelet transform corresponding to the Hermitian symmetry of the wedges θ_l and $\theta_l + \pi$ in the frequency domain. There are two different ways to evaluate the integral (C) efficiently. In this paper, we use the implementation via wrapping *i.e.* the digital coronisation with shears introduced in [20]. This fast digital Curvelet transform is a numerical isometry. We refer to [20] for further details and to Curvelab package² for the 2D and 3D implementation.

4.2. Fully wedge restricted Curvelets. Let $\mathbf{k}_\theta \in \mathbb{R}^d$ be Curvelet wavefront vector corresponding to the orientation $\theta \in [-\pi, \pi)^{d-1}$ and $\hat{\mathbf{k}}^i \in \mathbb{R}^d$ a unit vector along the i th coordinate direction. In 2D $\theta = \angle(\hat{\mathbf{k}}^1, \mathbf{k}_\theta) \in [-\pi, \pi)$ is just a single angle, in 3D we have 2 angles and in \mathbb{R}^d , $d-1$ angles. The *wedge restricted Curvelet transform*³ [45] amounts to computing the directional Curvelet coefficients (C) only for a wedge-shaped subset of angles $\theta_l \in [\theta_b, \theta^t] \cup [-\pi, \pi)^{d-1}$. The *symmetric wedge restricted Curvelet transform* restricts the Curvelet

²<http://www.curvelet.org/software.html>

³https://github.com/BolinPan/Wedge_Restricted_Curvelet

orientations to the symmetric double wedge (bow-tie) $\theta_l \in W := [-\theta^w, \theta^w] \cup [-\theta^w + \pi, \theta^w + \pi]$ with $\theta^w \in (0, \pi/2)^{d-1}$ as illustrated in Figure 4 (b) for 2D, where the gray region corresponds to the Curvelet with orientations inside the bow-tie range.

The drawback of the original formulation of the wedge restricted Curvelet transform are the isotropic Wavelet window functions at the coarse scale inherited from the original Curvelet transform which result in non-directional coarse scale coefficients. To overcome this shortcoming, we enforce the split into in and out of wedge frequencies also at the coarse scale j_0 by applying a binary bow-tie filter to the coarse scale in Fourier domain, and henceforth we refer to this construction as a *fully wedge restricted Curvelet transform*⁴. Formally we can write the fully wedge restricted Curvelet transform $\check{\Psi} : \mathbb{R}^n \rightarrow \mathbb{R}^{\check{N}}$, $\check{N} < N$ as a composition of the standard Curvelet transform $\Psi : \mathbb{R}^n \rightarrow \mathbb{R}^N$ and a projection operator $P_W : \mathbb{R}^N \rightarrow \mathbb{R}^{\check{N}}$, $\check{\Psi} = P_W \Psi$

$$(4.1) \quad P_W : \mathbb{R}^N \rightarrow \mathbb{R}^{\check{N}}$$

$$P_W(C_{j,l}(\mathbf{a})) = \begin{cases} C_{j,l}(\mathbf{a}), & \theta_{j,l} \in W, j \geq j_0 \\ \mathbf{0}, & \text{otherwise,} \end{cases}$$

where the angles $\theta_{j,l}$ are the discrete wedge orientations (essentially corresponding to the wedge centres). We note the fully wedge restricted Curvelet transform is an isometry when defined on the restriction to the range of P_W i.e. $\check{\Psi} : \mathbb{R}^n|_{\text{range}(P_W)} \rightarrow \mathbb{R}^{\check{N}}$, where $\text{range}(P_W)$ corresponds to the set W in the Fourier domain. Figure 4 (b,c) illustrate the difference between the Fourier domain ranges of the wedge restricted and fully wedge restricted Curvelet transforms in 2D.

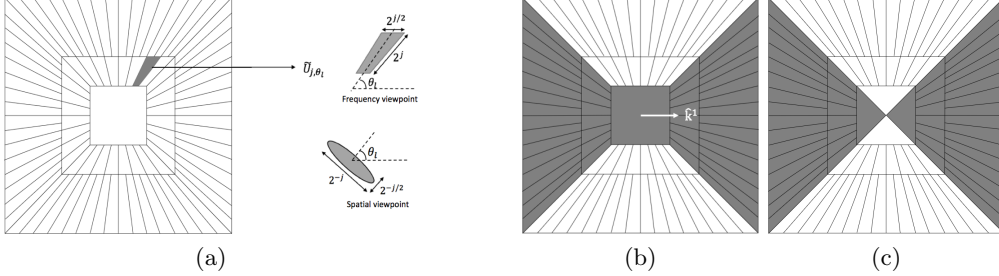


Figure 4: (a) An example of a 2D frequency domain Curvelet tiling using 3 scales. The highlighted wedge, magnified view in top right, corresponds to the frequency window near which the Curvelet \tilde{U}_{j,θ_l} at the scale j with orientation θ_l is supported. The orientation of the envelope of the corresponding Curvelet function in the spatial domain is shown in bottom right corner. Induced (b) wedge restricted (c) fully wedge restricted Curvelet transforms for $\theta_{\max} = \pi/4$. The respective bow-tie shaped ranges are coloured gray.

4.3. Fully wedge restricted Curvelet representation of initial pressure. Curvelets provide an almost optimally sparse representation if the function $u : \mathbb{R}^d \rightarrow \mathbb{R}$ is smooth away

⁴<https://github.com/BolinPan/CoronaeNet>

from (piecewise) \mathcal{C}^2 singularities [22, 55, 24]. More precisely, the error of the best s -term approximation, u_s , (corresponding to taking the s largest in magnitude coefficients) in Curvelet frame decays as [22]

$$(4.2) \quad \|u - u_s\|_2^2 \leq \mathcal{O}((\log s)^3 \cdot s^{-2}).$$

Furthermore, Curvelets have been shown to sparsely propagate through the wave equation [21] essentially being translated along the trajectories of the Hamiltonian flow with initial conditions corresponding to the spatial domain centre and the direction of the Curvelet. For constant speed of sound, this implies that the angle θ at which the Curvelet impinges on the detector is the same as the Curvelet orientation in the decomposition of the initial pressure p_0 . A direct consequence of the restriction of the angle $|\theta| \leq \theta_{\max}$ is the restriction to the *visible* initial pressure p_0 , which corresponds to symmetric fully wedge restricted Curvelet transform with directions $\theta_l \in W_{\max}^\theta$, $W_{\max}^\theta := [-\theta_{\max}, \theta_{\max}] \cup [-\theta_{\max} + \pi, \theta_{\max} + \pi]$ with $\theta_{\max} \in (0, \pi/2)^{d-1}$. On the other hand, the restriction of the impingement angle, $|\theta| \leq \theta_{\max}$, translates via (WfM) into the restriction of the angle β , $|\beta| \leq \arctan(\sin \theta_{\max})$, implying narrowing of the bow-tie shaped range of the PAT forward operator to $W_{\max}^\beta := [-\beta_{\max}, \beta_{\max}] \cup [-\beta_{\max} + \pi, \beta_{\max} + \pi]$ with $\beta_{\max} = \arctan(\sin \theta_{\max}) \in (0, \pi/4)^{d-1}$.

We now reinterpret (C) to obtain the symmetric fully wedge restricted Curvelet transform for representation of the *visible* initial pressure

$$(\text{FWRC}) \quad \check{C}_{j,l}(\mathbf{a}_\perp, \mathbf{a}_S) = \iint_{\mathbb{R}^d} \hat{u}(\mathbf{k}_\perp, \mathbf{k}_S) \tilde{U}_{j,\theta_{j,l}}(\mathbf{k}_\perp, \mathbf{k}_S) e^{i(\mathbf{x}_a \cdot (\mathbf{k}_\perp, \mathbf{k}_S))} d\mathbf{k}_\perp d\mathbf{k}_S, \quad \theta_{j,l} \in W_{\max},$$

with the following notation

- ($\mathbf{k}_\perp, \mathbf{k}_S$) ambient/image domain frequency $\mathbf{k} = (\mathbf{k}_\perp, \mathbf{k}_S)$;
- ($\theta_{j,l}$) a discrete direction of a trapezoidal frequency window $\tilde{U}_{j,\theta_{j,l}}(\mathbf{k}_\perp, \mathbf{k}_S)$. The tiling is computed using standard Curvelet transform on a cuboid domain, followed by the projection P_W on the bow-tie shaped set W_{\max} ; We remark, that efficient implementation would bypass the computation of the wedges outside W_{\max} , but it would require modifications to the Curvelet Toolbox functions.
- (W_{\max}) the restriction of $\theta_{j,l}$ to those in the bow-tie $W_{\max} := [-\theta_{\max}, \theta_{\max}] \cup [-\theta_{\max} + \pi, \theta_{\max} + \pi]$ with $\theta_{\max} \in (0, \pi/2)^{d-1}$ effects the projection on the *visible* range of initial pressure in Fourier domain;
- ($\mathbf{a}_\perp, \mathbf{a}_S$) the grid of spatial translations: \mathbf{a}_S parallel to the detector S , \mathbf{a}_\perp perpendicular to S (note that Curvelet transform via wrapping uses one grid per each quadrant at each scale, a.k.a. $\mathbf{x}_a^{j,\mathbb{Q}} = (2^{-j} \mathbf{a}_\perp^\mathbb{Q}, 2^{-j/2} \mathbf{a}_S^\mathbb{Q})$, $\mathbb{Q} = \{\mathbb{N}, \mathbb{W}, \mathbb{S}, \mathbb{E}\}$).

We note that in practice, the function $p_0 : \mathbb{R}^d \rightarrow \mathbb{R}$ is discretised on an n point grid in \mathbb{R}^d , yielding a vector $p_0 \in \mathbb{R}^n$, and we apply the symmetric discrete Curvelet transform $\Psi : \mathbb{R}^n \rightarrow \mathbb{R}^N$. The discrete counterparts of the wedge restricted $\tilde{\Psi}$ and fully wedge restricted $\check{\Psi}$ transforms follow analogously.

We compare the standard Curvelet transform Ψ , wedge restricted Curvelet transform $\tilde{\Psi}$ with fully wedge restricted Curvelet transform $\check{\Psi}$ for $\theta_{\max} = \pi/4$ on the 4-disk phantom (shown in Figure 3 (a)). We use 3 scales and 32 angles (at the 2nd coarsest level) for the standard Curvelet transform, yielding wedge restricted transforms with 16 angles (at the 2nd coarsest

level). Both the wedge restricted Curvelet transform and the fully wedge restricted Curvelet transforms exclude the wedges out of the bow-tie range W_{\max} at the higher $j > j_0$ scales; see Figure 5 (b,c). The standard Curvelet transform and the wedge restricted Curvelet transform have the same coarse scale coefficients while the fully wedge restricted Curvelet transform enforces the the split of the coarse scale into visible $\theta_{j,l} \in W_{\max}$ and invisible $\theta_{j,l} \notin W_{\max}$ to obtain the visible initial pressure only; see Figure 5 (d-f).

The projections effected by all three Curvelet transforms are shown in Figure 6. Figure 6 (c,f) illustrates that the projection on the range of fully wedge restricted Curvelet transform corresponds to the visible initial pressure.

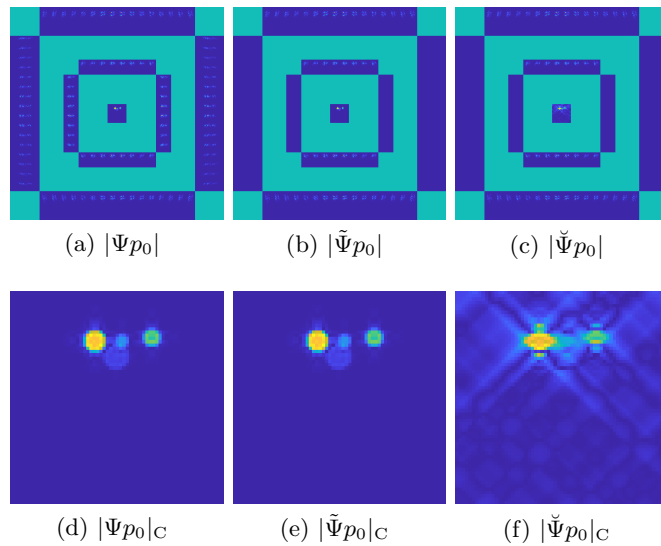


Figure 5: 4-disk Phantom - Curvelet coefficients of 4-disk phantom ($\theta_{\max} = \pi/4$ for wedge restriction): (a) standard, (b) wedge restricted, (c) fully wedge restricted Curvelet transform coefficient magnitudes; (d-f) the corresponding coarse scale coefficients.

5. Reconstructing the visible and learning the invisible. The fully wedge restricted Curvelet transform introduced in subsection 4.3 allows us to decompose the initial pressure $p_0 \in \mathbb{R}^n$ into Curvelet coefficients that belong to either the visible $f^{\text{vis}} \in \mathbb{R}^{\check{N}}$ or the invisible $f^{\text{inv}} \in \mathbb{R}^{\check{N}}$ initial pressure (in the sense that the other coefficients are set to 0)

$$\begin{aligned} \text{(VID)} \quad f^{\text{vis}} &= \check{\Psi}p_0, \\ f^{\text{inv}} &= \check{\Psi}^\perp p_0. \end{aligned}$$

Given the limited-view data $g_\angle \in \mathbb{R}^m$ contaminated with additive white noise, the *visible* initial pressure p_0 can be reconstructed by reconstructing the *visible* coefficients of p_0 in the fully wedge restricted Curvelet frame. The latter is a standard compressed sensing $\ell_2 - \ell_1$ minimisation problem with the ℓ_2 data fidelity term involving the aforementioned limited-angle PAT Fourier forward operator. As the invisible coefficients are out of range of the

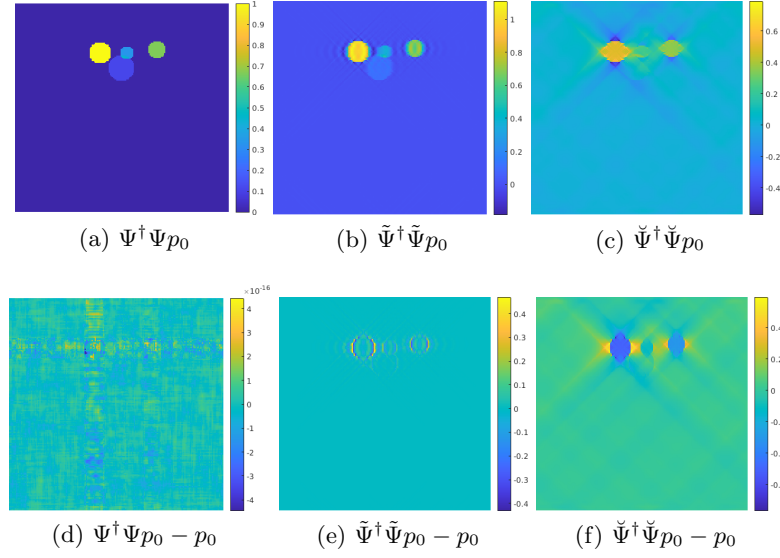


Figure 6: 4-disk Phantom - Visualisation of projection effected by the different types of Curvelet transform ($\theta_{\max} = \pi/4$ for wedge restriction): projection on the range of (a) standard Ψ , (b) wedge restricted $\tilde{\Psi}$, (c) fully wedge restricted $\check{\Psi}$; (d-f) projection on corresponding range complements in \mathbb{R}^d .

forward operator *i.e.* $f^{\text{inv}} \in \ker(\hat{\mathbf{A}}_{\angle})$ [27], f^{inv} can not be reconstructed from g_{\angle} . Instead we can recover the invisible coefficients using a trained CNN. We refer to such two step method as *reconstructing the visible and learning the invisible*.

5.1. Reconstructing the Visible. In this step, we recover the visible part of initial pressure $p_0 \in \mathbb{R}^n$ from noisy measurement $g_{\angle} \in \mathbb{R}^m$ in a fully wedge restricted Curvelet frame. To this end we solve

$$(\mathbf{VR}) \quad \tilde{f}^{\text{vis}} \in \arg \min_f \frac{1}{2} \|\hat{\mathbf{A}}_{\angle} \check{\Psi}^{\dagger} f - \hat{g}_{\angle}\|_2^2 + \tau \|\Lambda f\|_1,$$

where $\hat{\mathbf{A}}_{\angle} : \mathcal{D}_{\mathbf{A}}^{\angle} \rightarrow \mathcal{R}_{\mathbf{A}}^{\angle}$ is the discrete limited-angle PAT Fourier forward operator, $\check{\Psi}^{\dagger} : \mathbb{R}^{\check{N}} \rightarrow \mathbb{R}^n$ is the left inverse (and an adjoint) of the fully wedge restricted Curvelet transform $\check{\Psi}$ ⁵, f are the coefficients of p_0 in $\check{\Psi}$, \tilde{f}^{vis} are the reconstructed visible Curvelet coefficients, and the regularisation parameter τ is made scale dependent by multiplication with $\Lambda = \text{diag}(2^{j-2})$, where $j \geq j_0$ is the vectors containing the scales of the basis elements $\check{\Psi}$. We propose to solve **(VR)** using **FISTA** [12] with a pre-computed Lipschitz constant $L = \|\check{\Psi} \hat{\mathbf{A}}_{\angle}^{\dagger} \hat{\mathbf{A}}_{\angle} \check{\Psi}^{\dagger}\|_2$.

5.2. Learning the invisible. Armed with the visible reconstruction f^{vis} , we now learn the invisible coefficients by a tailored U-Net. As the invisible coefficients are out of range of the

⁵As already mentioned in [section 3](#) all the computations can be executed directly in Fourier domain. For simplicity we use the same notation for transforms $(\Psi, \tilde{\Psi}, \check{\Psi})$, which act on the Fourier transform \hat{p}_0 as for those that act on p_0 itself.

forward operator, there is no need/benefit to include the forward and adjoint operators into the network. Our network is based on U-Net architecture, which we refer to as *Coronae-Net* (CorNet) is depicted in Figure 10. We use the *Coronae Decomposition* in lieu of downsampling and the *Coronae Reconstruction* in lieu of upsampling. The input of CorNet are visible Coronae coefficients which are generated from the reconstructed visible Curvelet coefficients. The visible Coronae coefficients are mapped to a latent representation via a series of convolutions, non-linearities and high/low-pass filters on the down branch of the CorNet. The correlations between the visible and invisible part of the image are encoded in this latent representation during training and allow prediction of the invisible part of the image. The decoder branch of the CorNet, decodes and upsamples both visible and invisible Coronae coefficients to the highest scale output.

5.2.1. Coronae Decomposition and Reconstruction. The Coronae decomposition is motivated from the Curvelet transform, where the high-pass and low-pass filter bank is applied to effect the scale (frequency band) decomposition. Coronae decomposition is computed in Fourier domain but the Coronae coefficients at each scale are images obtain with inverse scale restricted Fourier transform. We make use of the same smooth partition of unity filters as used in Curvelet Toolbox. We henceforth denote the filter pair at scale j with \mathbb{L}_j the low-pass filter and $\mathbb{H}_j = \sqrt{1 - (\mathbb{L}_j)^2}$ the high-pass filter. For each scale j , the image p_j has the size

$$(5.1) \quad \left(\frac{n_J}{3 \cdot 2^{J-j-1}} + 2 \cdot \lfloor \frac{n_J}{3 \cdot 2^{J-j}} \rfloor + 1 \right) \times \left(\frac{m_J}{3 \cdot 2^{J-j-1}} + 2 \cdot \lfloor \frac{m_J}{3 \cdot 2^{J-j}} \rfloor + 1 \right),$$

where $j_0 \leq j < j_0 + J$ and $n_J \times m_J$ is the image size of p_{j_0+J} . $\mathbb{H}_j(p_j)$ returns the high-pass component with the same size as p_j and $\mathbb{L}_j(p_j)$ the low-pass component with the size of p_{j-1} ; see Figure 8 for visualisation of the effect of 1-level of Coronae decomposition of the 4-disk phantom. The Fourier domain computations involved in Coronae decomposition are schematically shown in Figure 7 (where for visualisation purposes the overlapping smooth partition of unity filters⁶ are replaced with discontinuous non-overlapping partition of unity by characteristic function of the pass-through). The signal can be recovered by the Coronae reconstruction. The Coronae reconstruction upsamples the low-pass component via zero-padding and sums up the padded low-pass component with the corresponding high-pass component in Fourier domain to recover the original signal (denoted with \oplus). Based on this 1-level Coronae decomposition effected by the pair $(\mathbb{L}_j, \mathbb{H}_j)$ we can form a filter bank via recursion for the decomposition

$$(5.2) \quad ((\mathbb{L}_{j-1}(\mathbb{L}_j), \mathbb{H}_{j-1}(\mathbb{L}_j)), \mathbb{H}_j), \quad j = j_0 + J, \dots, j_0 + 1,$$

and for the reconstruction

$$(5.3) \quad (\mathbb{L}_{j-1} \oplus \mathbb{H}_{j-1}) \oplus \mathbb{H}_j, \quad j = j_0 + 1, \dots, j_0 + J,$$

Figure 7 (right) displays a 3 scale filter bank where the red and green arrows indicate the Coronae decompositions and reconstructions, respectively.

⁶Such filters require appropriate wrapping of the low pass component $\mathbb{L}_j(p_j)$ before Fourier inversion at scale $j - 1$.

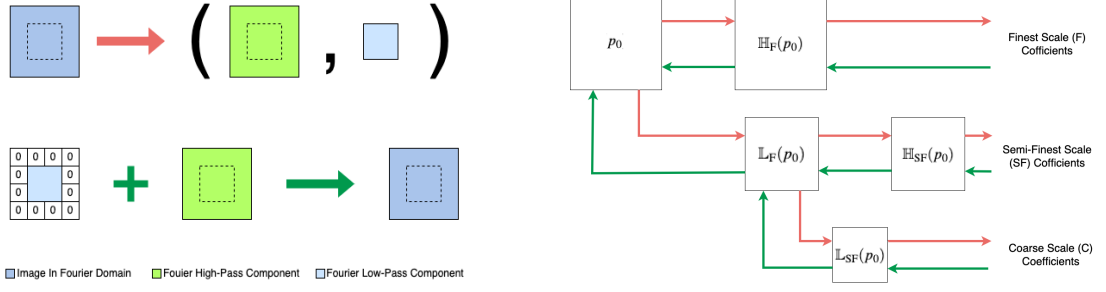


Figure 7: Left: 1-level Coronae decomposition in 2D Fourier domain. Coronae decomposition (top), and reconstruction using zero padding (bottom). Right: a filter bank with 3 scales effecting 2-levels Coronae decomposition (\rightarrow) and reconstructions (\leftarrow).

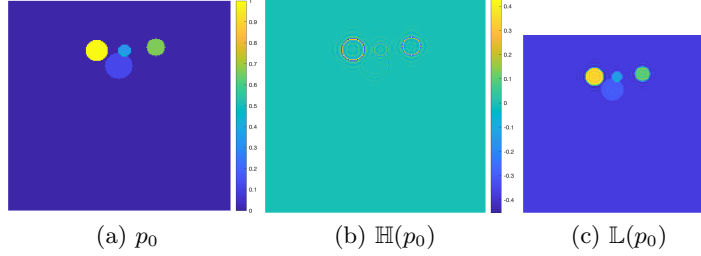


Figure 8: 1-level Coronae decomposition of a 4-disk phantom: (a) p_0 , (b) high-pass component $\mathbb{H}(p_0)$, and (c) low-pass component $\mathbb{L}(p_0)$.

5.2.2. Rationale for Using Coronae Coefficients as Network Input. There are two disadvantages to usage of individual Curvelets as a network input. Firstly, to preserve the locality of the CNN convolutions (with kernels with localized support, frequently 2 or 3 pixels), they need to be applied in image domain. In the most straightforward realisation, this would required computing an image domain representation of each individual Curvelet $\Psi^\dagger(C_j(\mathbf{a})), j \geq j_0$ (see Figure 9 (a-c)) which, even when using scale appropriate image sizes, would result in a prohibitive number of image inputs. A better alternative is to use the images of each individual trapezoidal wedge window (as are used for displaying the Curvelet coefficients c.f. Figure 5). However, these are still numerous due to parabolic scaling induced doubling every second scale. Furthermore, their size varies even within the scale which would require additional processing e.g. zero-padding. We are however, interested in the split into visible and invisible parts rather than in individual Curvelet coefficients. This is most economically represented by the Coronae decomposition applied to the visible/invisible parts of the image (see Figure 9 (d,e) which results in two channel input (visible and invisible channel)). Secondly, it is apparent from Figure 9 that Coronae decomposition is a more economic and a higher level feature representation, as it is not reliant on a superposition for final representation unlike Curvelet decomposition. Thus we can reasonably expect it will be easier to learn.

The relation of the Coronae and Curvelet decompositions can be formally stated in Fourier domain as

$$(\mathbf{QC}) \quad \hat{Q}_j(\mathbf{k}_j) = \sum_l \int_{\mathbb{R}^d} C_{j,l}(\mathbf{a}_{j,l}) e^{-i\mathbf{x}_{\mathbf{a}_{j,l}} \cdot \mathbf{k}_j} d\mathbf{a}_{j,l},$$

where \mathbf{k}_j is the frequency domain vector restricted to scales $j \geq j_0$ ⁷ and $\mathbf{x}_{\mathbf{a}_{j,l}}$ are the Curvelet centers at scale j and angle $\theta_{j,l}$. In particular, when using implementation via wrapping we have one grid per quadrant $\mathbf{x}_{\mathbf{a}_{j,l}} = \mathbf{x}_{\mathbf{a}_{j,\mathbb{Q}(l)}}$. The coarse scale Coronae and Curvelet coefficients coincide.

In what follows Coronae transform will be applied to the visible and invisible parts of the image which corresponds to restricting the sum in **(QC)** to the visible wedge W_{\max} or its complement for invisible coefficients. The implementation bypasses the computation of the Curvelet transform. After Fourier domain application of the bow-tie shaped filter to extract the visible $\mathbf{k} \in W_{\max}$ and its complement the invisible $\mathbf{k} \notin W_{\max}$, we use the filters bank define in [subsection 5.2.1](#) to obtain the Coronae decomposition Q of each visible/invisible component directly. Figure 9 (d-f) shows 2-level Coronae decomposition coefficients of the 4-disk phantom.

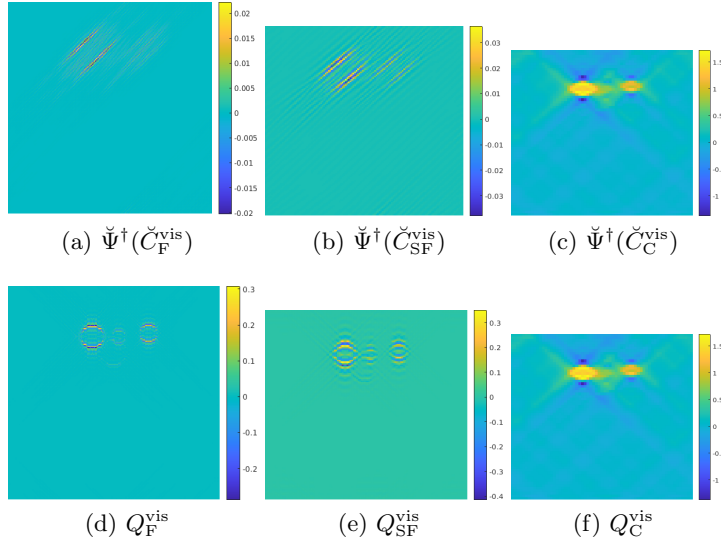


Figure 9: 4-disk Phantom - Spatial representation of visible Curvelet coefficients (a-c) and of visible Coronae coefficients (d-f) at scales $\{C, SF, F\}$ ($\theta_{\max} = \pi/4$).

5.2.3. Coronae-Net. We propose a following *Coronae-Net* (CorNet) which we construct with a depth matching the number of scales of the Curvelet decomposition. The input at each scale j consists of 2 channels: the first channel is the Coronae coefficient $Q_j(p^{\text{vis}})$ of

⁷Note that the overlapping smooth partition of unity filters yield larger \mathbf{k}_j than the 0-1 non-overlapping filters.

the visible and the second channel will be used to predict the unknown Coronae coefficient $Q_j(p^{\text{inv}})$ of the invisible. At the input stage the latter could be initialised with $\mathbf{0}$ but in practice adding random white noise in training is preferable. In the encoder branch, scale by scale the convolutions and nonlinearities extract and correlate the features of the visible and invisible Coronae coefficients to effect the prediction of the invisible Coronae coefficients. The Coronae decomposition is used to pass the low-pass components downward and high-pass components directly to the decoder via the skip connection. On the up-branch the visible and predicted invisible features are decoded via a symmetric cascade of convolutions and nonlinearities. The Coronae reconstruction is used assemble the high-pass components passed through the skip connection with the low-pass components obtained from the deeper layer. We highlight the asymmetry in the CorNet input and output, while we input the Coronae coefficients scale-wise, the output Coronae coefficients are upsampled (via 0-padding) and returned at the finest scale. Furthermore, the output is multi-headed, as popular in multi-task learning framework, which allows us to assign different weights to coefficients at different scales (and possibly even to visible and invisible channels).

Although the output contains both visible and invisible, the loss function is only applied to the invisible Coronae coefficients and can be written as

(PL)

$$\mathcal{L}(\mathcal{NN}_{\text{Cor}}(Q^{\text{P}_{\text{vis}}}), \tilde{Q}^{\text{P}_{\text{inv}}}) = \sum_j \left(\alpha_j \cdot \text{MSE} \left(\mathcal{NN}_{\text{Cor}}(Q_j^{\text{P}_{\text{vis}}}), \tilde{Q}_j^{\text{P}_{\text{inv}}} \right) \right), \quad j \in \{j_0, \dots, j_0 + J\},$$

where the perfect visible Coronae coefficients (original size) $Q_j^{\text{P}_{\text{vis}}}$ are the input to the CorNet, $\mathcal{NN}_{\text{Cor}}$, $\tilde{Q}_j^{\text{P}_{\text{inv}}}$ are the upsampled to the finest-scale perfect/reference invisible Coronae coefficients, and α_j are some fixed scale dependent weights. The total loss (PL) is summed over the training set of in/output pairs of $Q^{\text{P}_{\text{vis}}}$ and $\tilde{Q}^{\text{P}_{\text{inv}}}$.

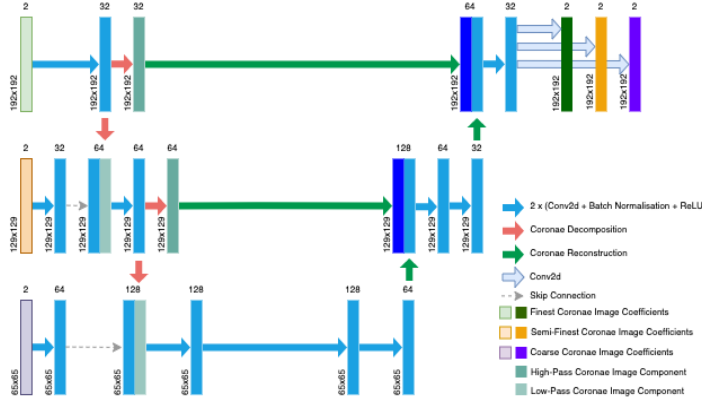


Figure 10: Coronae-Net - Architecture here shown with 3 scales for learning the invisible Coronae coefficients in 2D. The Coronae decomposition and reconstruction are used as down-sampling and up-sampling in the network, respectively.

Recall the invisible Curvelet coefficients are in the kernel of the limited-angle PAT Fourier

forward operator. The same holds for invisible Coronae coefficients, c.f. subsection 5.2.2 thus learning the invisible with CorNet from perfect visible coefficients also follows a null space learning paradigm as the scheme presented in [49], but our chosen representation is essentially optimal for both the image representation and the PAT forward operator.

$$Q^{P_{\text{vis}}} + P_{\ker(\hat{\mathbf{A}}_{\angle})} \mathcal{NN}_{\text{Cor}}(Q^{P_{\text{vis}}}),$$

where $P_{\ker(\hat{\mathbf{A}}_{\angle})}$, the projection on $\ker(\hat{\mathbf{A}}_{\angle})$, extracts the invisible output channel.

5.2.4. ResCoronae-Net. The main limitation of the perfect/null space learning is the assumption of availability of perfect visible coefficients. In realistic scenarios the reconstructed visible Coronae coefficients Q^{vis} will suffer from artefacts introduced by the reconstruction procedure. In our case, the Fourier operators contain an error due to interpolation between image and data domain grids. Therefore, we propose a residual version of the Coronae-Net, *ResCoronae-Net* (ResCorNet), to learn an update to both visible and invisible Coronae coefficients. We use the same **0** or random noise initialisation for the invisible coefficients as for CorNet, thus the residual connection has no effect for invisible coefficients. We note that we need to upsample our inputs to the finest scale to match the output size before the residual connections (the diagram of ResCoronae-Net can be found in supplementary material Figure SM1). The loss function used for the residual learning penalises errors in both visible and invisible Coronae coefficients

(**IPL**)

$$\mathcal{L}(\mathcal{NN}_{\text{ResCor}}(Q^{\text{Ivis}}), \tilde{Q}^{P_{\text{all}}}) = \sum_j \left(\alpha_j \cdot \text{MSE} \left(\mathcal{NN}_{\text{ResCor}}(Q_j^{\text{Ivis}}), \tilde{Q}_j^{P_{\text{all}}} \right) \right), \quad j \in \{j_0, \dots, j_0 + J\},$$

where the reconstructed imperfect visible Coronae coefficients (original size) Q_j^{Ivis} are the input to the ResCorNet, $\mathcal{NN}_{\text{ResCor}}$, $\tilde{Q}_j^{P_{\text{all}}}$ are the upsampled to the finest-scale perfect/reference visible and invisible Coronae coefficients, and α_j some fixed scale dependent weights. Again, the total loss (**IPL**) is summed over the training set of in/output pairs of Q^{Ivis} and $\tilde{Q}^{P_{\text{all}}}$.

6. Synthetic Data. In this section, we evaluate the performance of our proposed reconstruction scheme and compare it with various other reconstruction methods. We focus on two learning scenarios: 1) *Perfect Learning*, learns the invisible Coronae coefficients from the given perfect visible Coronae coefficients via CorNet with loss function (**PL**); 2) *Imperfect Learning*, learns the update of the visible and the invisible Coronae coefficients, from the imperfect visible Coronae coefficients, constructed from the solution of (**VR**), via ResCorNet with loss function (**IPL**).

6.1. Experimental Setup. We evaluate our proposed method on an *ellipse data set*. The data consists of 3000 synthetic images of superposition of random ellipses (number, location, orientation and contrast) with resolution of $n_{\mathbf{x}_{\perp}} \times n_S = 192 \times 192$ and a uniform voxel size $h_{\mathbf{x}} = 10\mu\text{m}$. The locations of the ellipses are randomly chosen within the upper half of the image to reduce (while not eliminate completely) the limited sensor effect. The individual images are normalised between 0 and 1 (see Figure 11 (a) for a representative image sample from the ellipse data set).

We assume homogeneous speed of sound $c = 1500\text{m/s}$. The pressure time series is recorded every $h_t = 66.67\text{ns}$ by a line sensor with sensitivity angle $\theta_{\max} = \pi/4$ on top of the domain with image matching resolution *i.e.* $h_x = 10\mu\text{m}$, which we can interpret as number of time-steps \times number of sensors shaped PAT data volume, 272×192 .

We use the fully wedge restricted Curvelet transform with 3 scales and 16 angles in the wedge W_{\max} (at the 2nd coarse scale) for the sparse representation of initial pressure p_0 . The parameters of the transform determine the structure of the networks such as depth (equal to the number of scales, here 3), and the input/output sizes.

We trained all the networks presented in this section in the same manner to make a fair comparison. 2400 images are used for training, 300 images for validation and 300 for testing. We chose Adam as the optimizer with Xavier initialisation [31] and batch size of 2. We trained all networks for 200 epochs with 20 epochs early stopping to avoid over-fitting. The initial learning rate is set to $1 \cdot 10^{-3}$ with a cosine decay. Each network is trained in PyTorch on a single Tesla K40c GPU.

6.2. Perfect Learning. We start with an idealised experiment where we learn the invisible Coronae coefficients from the perfect visible Coronae coefficients. The perfect visible/invisible image components and Coronae coefficients of each image p_0 in the data set are computed directly via projections $p_0^{\text{P}_{\text{vis}}} = \check{\Psi}^\dagger \check{\Psi} p_0$, $p_0^{\text{P}_{\text{inv}}} = p_0 - \check{\Psi}^\dagger \check{\Psi} p_0$ or Coronae decomposition or p_0 .

The variation in magnitudes and sizes of Coronae coefficients across scales, suggests use of larger weights for higher scales. The choice of $\alpha_F = 2$, $\alpha_{SF} = 2$ and $\alpha_C = 1$ in (PL) lead to best network performance. We quantitatively compare the results of CorNet with standard variational approaches and U-Net based learned post-processing on the ellipse test data, in terms of MSE, PSNR and SSIM averaged over the test set.

We compare our results to two reference learned post-processing methods, based on U-Net architecture, trained to remove limited-view artefacts. $\mathcal{NN}_{\text{U-Net}}(p_0^{\text{P}_{\text{vis}}})$ takes as an input the perfect visible component $p_0^{\text{P}_{\text{vis}}}$ and is trained on $(p_0^{\text{P}_{\text{vis}}}, p_0)$ pairs with MSE loss. $\mathcal{NN}_{\text{U-Net}}(\tilde{Q}_j^{\text{P}_{\text{vis}}})$ takes as an input the upsampled to the finest scale (via zero-padding in Fourier domain) perfect visible Coronae coefficients $\tilde{Q}_j^{\text{P}_{\text{vis}}}$ (a.k.a. multichannel input at highest scale only, one channel per scale) and is trained on $(\tilde{Q}_j^{\text{P}_{\text{vis}}}, \tilde{Q}_j^{\text{P}_{\text{all}}})$ pairs with MSE loss. The diagrams of the reference U-Nets can be found in supplementary material.

Table 1: Ellipses - Map from perfect visible to invisible. Imaging metrics averaged over the test set.

	MSE	PSNR	SSIM
$p_0^{\text{P}_{\text{vis}}}$	$5.8311 \cdot 10^{-3} \pm 2.0110 \cdot 10^{-3}$	22.6029 ± 1.5361	0.3612 ± 0.0547
$p_0^{\text{P}_{\text{inv}}}$	$1.5827 \cdot 10^{-2} \pm 5.0783 \cdot 10^{-3}$	18.2206 ± 1.3726	0.2729 ± 0.0574
$\mathcal{NN}_{\text{U-Net}}(p_0^{\text{P}_{\text{vis}}})$	$1.2207 \cdot 10^{-4} \pm 5.4004 \cdot 10^{-5}$	39.5088 ± 1.7885	0.9889 ± 0.0044
$\mathcal{NN}_{\text{U-Net}}(\tilde{Q}_j^{\text{P}_{\text{vis}}})$	$5.1026 \cdot 10^{-5} \pm 2.4257 \cdot 10^{-5}$	43.3695 ± 1.9730	0.9907 ± 0.0038
$\mathcal{NN}_{\text{Cor}}(Q_j^{\text{P}_{\text{vis}}})$	$3.4599 \cdot 10^{-5} \pm 1.4536 \cdot 10^{-5}$	44.9678 ± 1.7715	0.9919 ± 0.0030

A visualisation of the reconstruction quality for one of the test images is given in Figure 11. The first row of Figure 11 displays the initial pressure p_0 along with its decomposition into perfect visible $p_0^{\text{P}_{\text{vis}}}$ and perfect invisible $p_0^{\text{P}_{\text{inv}}}$ parts. The second row of Figure 11 illustrates

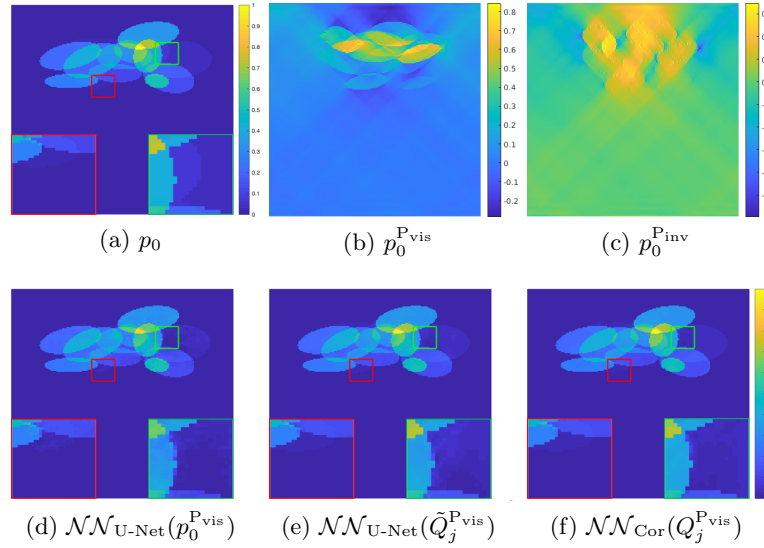


Figure 11: Ellipses - Visualisation of performance of perfect learning on one test image ($\theta_{\max} = \pi/4$): (a) the initial pressure p_0 , (b) the perfect visible component of p_0 , (c) the perfect invisible component of p_0 , (d-f) different learned reconstructions.

the learned reconstructions (pixel values clipped to $[0,1]$ range). Although all three methods perform very well, the zoomed-in insets in Figure 11 reveal our proposed scheme yields superior reconstruction in terms of invisible boundary (green inset), ellipse shapes and faint contrasts (red inset). On average, $\mathcal{NN}_{\text{Cor}}(Q_j^{\text{Pvis}})$ achieves lowest MSE, highest PSNR and highest SSIM in Table 1 which is consistent with better, in eye ball metric, reconstructions produced by the CorNet⁸. However, we observe all methods in (d-f) fail to recover the faint ellipse on top of even fainter large ellipse and overlapping with ellipses with higher contrasts (highlighted in green inset). The low contrast boundary of the faint ellipse is difficult to pick up for the networks. We encountered a similar scenario in Figure 8, where the boundary of the faint blue ellipse is almost invisible in the high-pass component $\mathbb{H}(p_0)$ while the boundaries of the ellipses with higher contrast are still perceptible.

6.3. Imperfect Learning. Next, we consider the more practical scenario of correcting the visible and learning the invisible Coronae coefficients on the ellipse data set from PAT data with additive white noise with standard deviation $\sigma = 2.5 \cdot 10^{-4}$. We reconstruct the visible Curvelet coefficients \hat{f}^{vis} solving (VR) with regularisation parameter $\tau = 2.5 \cdot 10^{-4}$ and 50 iterations. This scenario employs ResCorNet with the scale dependent loss weights $\alpha_F = 2$, $\alpha_{SF} = 2$ and $\alpha_C = 1$ in (IPL). Again we compare the results obtained with ResCorNet against and residual variants of U-Net learned post-processing methods on the test subset of ellipse data.

We compare our results to five reference methods. $p_0^{\text{Linear}} = \hat{\mathbf{A}}_{\angle}^{-1} g_{\angle}$: linear inversion from

⁸The invisible Coronae coefficients $\tilde{Q}_j^{\text{Linv}}$ learned using CorNet can be found in supplementary material.

noisy limited-view data g_\angle . $p_0^{\ell_1^{\text{vis}}}$: recovery of the visible part of p_0 in fully wedge restricted Curvelet frame via (VR). $p_0^{\text{TV+}^{\text{vis}}}$: total variation regularised solution with non-negativity constraint [8]. And two learned post-processing methods based on ResU-Net architecture trained to remove artefacts due to limited angle and errors in the visible Coronae coefficients. $\mathcal{NN}_{\text{ResU-Net}}(p_0^{\text{vis}})$: takes as an input the imperfect visible coefficients p_0^{vis} and is trained on (p_0^{vis}, p_0) pairs with MSE loss. $\mathcal{NN}_{\text{ResU-Net}}(\tilde{Q}_j^{\text{vis}})$: takes as an input the (upsampled to the finest scale via zero-padding in Fourier domain) imperfect visible Coronae coefficients \tilde{Q}_j^{vis} and is trained on $(\tilde{Q}_j^{\text{vis}}, \tilde{Q}_j^{\text{Pall}})$ pairs with MSE loss. The diagrams of the reference ResU-Nets can be found in supplementary material.

Table 2: Ellipses - Map from imperfect visible to corrected visible and learned invisible. Imaging metrics averaged over test set. Note, in the top two rows perfect visible component p_0^{Pvis} is used as a ground truth while in the remaining rows we use the original image p_0 .

	MSE	PSNR	SSIM
p_0^{Linear}	$1.5031 \cdot 10^{-4} \pm 6.0914 \cdot 10^{-5}$	38.5706 ± 1.7347	0.8296 ± 0.0460
$p_0^{\ell_1^{\text{vis}}}$	$9.5904 \cdot 10^{-5} \pm 3.6300 \cdot 10^{-5}$	40.4581 ± 1.5361	0.9577 ± 0.0090
p_0^{Linear}	$6.0860 \cdot 10^{-3} \pm 2.2048 \cdot 10^{-3}$	22.4308 ± 1.5593	0.3284 ± 0.0436
$p_0^{\ell_1^{\text{vis}}}$	$5.9660 \cdot 10^{-3} \pm 2.1752 \cdot 10^{-3}$	22.5209 ± 1.5700	0.3463 ± 0.0580
$p_0^{\text{TV+}}$	$8.6550 \cdot 10^{-5} \pm 4.4774 \cdot 10^{-5}$	41.0863 ± 1.9422	0.9861 ± 0.0059
$\mathcal{NN}_{\text{ResU-Net}}(p_0^{\text{vis}})$	$1.4197 \cdot 10^{-4} \pm 6.3716 \cdot 10^{-5}$	38.8494 ± 1.7685	0.9586 ± 0.0133
$\mathcal{NN}_{\text{ResU-Net}}(\tilde{Q}_j^{\text{vis}})$	$9.4125 \cdot 10^{-5} \pm 3.7918 \cdot 10^{-5}$	40.5950 ± 1.7027	0.9705 ± 0.0074
$\mathcal{NN}_{\text{ResCor}}(Q_j^{\text{vis}})$	$8.1092 \cdot 10^{-5} \pm 3.0781 \cdot 10^{-5}$	41.2081 ± 1.6141	0.9755 ± 0.0069

Table 3: Ellipses - Timing and resources for imperfect learning experiment.

	Train	Execution	Parameter
p_0^{Linear}	-	1m52s	0
$p_0^{\ell_1^{\text{vis}}}$	-	16m23s	1
$p_0^{\text{TV+}}$	-	14m12s	1
$\mathcal{NN}_{\text{ResU-Net}}(p_0^{\text{vis}})$	6h05m	~ 16s	467554
$\mathcal{NN}_{\text{ResU-Net}}(\tilde{Q}_j^{\text{vis}})$	8h12m	~ 24s	468838
$\mathcal{NN}_{\text{ResCor}}(Q_j^{\text{vis}})$	18h48m	~ 24s	1001670

The image quality measures averaged over the 300 test images are listed in Table 2, specifically MSE, PSNR and SSIM with respect to the provided ground-truth images. The reconstruction quality is illustrated on an example from the test set in Figure 12. Despite $p_0^{\text{TV+}^{\text{vis}}}$ achieving highest SSIM, the reconstructed boundaries of the ellipses highlighted in the white inset in Figure 12 (c) are incomplete (total variation apparently fails to completely recover the invisible boundaries) and considerably worse than for the learning based reconstructions (d-f). We note that the linear reconstruction p_0^{Linear} in Figure 12 (a) and $p_0^{\ell_1^{\text{vis}}}$ in Figure 12 (b) look similar with slight difference in contrast. The linear inversion results in slightly less clear ellipse boundaries and noisier image than the non-linear ℓ_1 reconstruction; see blue inset in Figure 12 (a,b). We recall, that the linear inversion here is able to recover the visible component due to limited-angle (and even limited sensor) completely, thus any

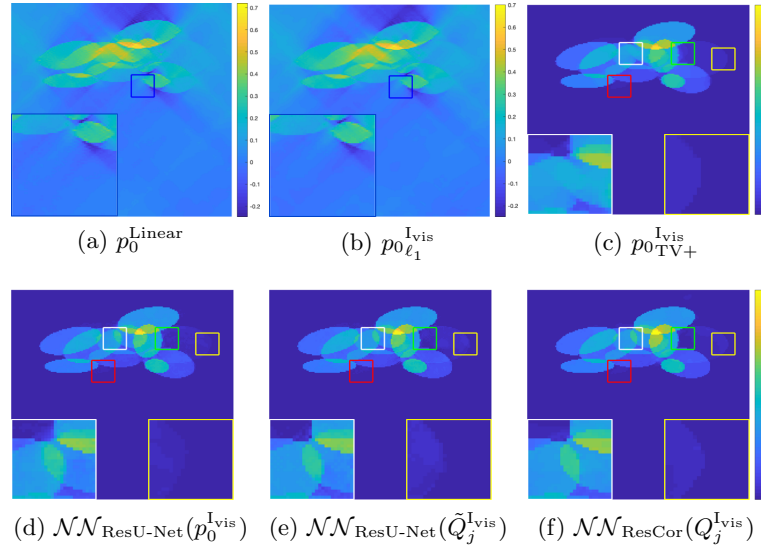


Figure 12: Ellipses - Visualisation of performance of the imperfect learning of one test image ($\theta_{\max} = \pi/4$): (a) the linear inversion of noisy limited-view data g_L , (b) the reconstructed imperfect visible component via **(VR)**, (c) total variation regularised solution with non-negativity constraint, (d-f) different learned reconstructions.

difference should be due to higher robustness of the non-linear reconstruction to noise. This is consistent with the latter's lower MSE, higher PSNR and higher SSIM compared to the linear inversion. The second row in Figure 12 (clipped to range $[0,1]$) shows the results of post-processing with ResU-Nets and ResCorNet, respectively. Although the ResU-Net based methods in Figure 12 (d,e) estimate the invisible boundaries reasonably well they exhibit some high frequency noise. Upon closer inspection (white and yellow insets Figure 12) and quantitative analysis in Table 2, our proposed ResCorNet seems to strike the best balance between the recovery of invisible boundaries while preserving the piece-wise constant interior of the ellipses. Similarly as in the perfect learning scenario, all three methods in (d-f) fail to recover the faint green framed ellipse.

The timing and resources are listed in Table 3 (Note p_0^{Ivis} and $p_0^{\text{Ivis}}_{\text{TV+}}$ are evaluated using Matlab Parallel Computing Toolbox⁹). Clearly $\mathcal{NN}_{\text{ResU-Net}}(p_0^{\text{Ivis}})$ is fastest to train and execute, while $\mathcal{NN}_{\text{ResCor}}(Q_j^{\text{Ivis}})$ requires longest training time. The main reason is due to ResCorNet's larger number of trainable parameters: 1) the preceding convolutions at each scale are paramount to extract the features from the scale-wise Coronae coefficients input; 2) the Coronae coefficients sizes are determined by the partition of unity filters underpinning Curvelet decomposition, which result in larger sizes of layer inputs at each but the finest scale than those obtained from max-pooling. It is noteworthy that at prediction stage, the approaches learning the Coronae coefficients $\mathcal{NN}_{\text{ResU-Net}}(\tilde{Q}_j^{\text{Ivis}})$ and $\mathcal{NN}_{\text{ResCor}}(Q_j^{\text{Ivis}})$ only

⁹<https://www.mathworks.com/products/parallel-computing.html>

have a slight overhead compared to $\mathcal{NN}_{\text{ResU-Net}}(p_0^{\text{I}_{\text{vis}}})$, and are much faster than the variational reconstruction approaches.

6.4. Generalisation. We now consider the generalisation properties of (Res)CorNet. To this end we chose an 4-disk phantom depicted in [Figure 13](#). The 4-disk phantom is not in the ellipse data set, while disk being a special case of an ellipse, it has similar features such as convexity and boundaries of C^2 type. In this experiment, the visible Curvelet coefficients are obtained solving **(VR)** with $\tau = 2.5 \cdot 10^{-4}$ and 50 iterations. Again the white noise with standard deviation $\sigma = 2.5 \cdot 10^{-4}$ is added to the corresponding limited-view data with $\theta_{\max} = \pi/4$. We apply the ResCorNet trained on the ellipse data set to the 4-disk phantom. This scenario corresponds to training on a complicated data set and generalising our model to a less complex image with some shared and some unseen characteristics. We note that the training set contains many ellipses at least partially outside the north sector of the domain (inside which the limited sensor has no bearing on the reconstruction) while our 4-disk phantom lies strictly inside. The main limitation of the ResU-Net based reconstructions in [Figure 13](#) (a,b) are streak like artefacts and failure to recover the invisible boundary of the large blue disk highlighted in magenta inset. Our proposed reconstruction method using ResCorNet in [Figure 13](#) (c) provides a notable improvement in the definition of the invisible boundary as well as the reduction in streak like background artefacts, which is consistent with its lowest MSE, highest PSRN and SSIM in [Table 4](#). However, even in (c) parts of the invisible boundary of the faint large blue disk are missing (both left and right sides). We believe these artefacts could be due to the training set containing images of many overlapping ellipses, which means that examples of boundaries against the background are rare, only present for exterior ellipses. Furthermore, we note that the recovered shape has some resemblance with an ellipse. Both observations testify to limits of generalisation. The remaining disks are almost perfectly reconstructed by all methods. Overall, our proposed method while not without limitations is clearly superior in this generalisation scenario both in eye ball metric and the quantitative analysis in [Table 4](#).

Table 4: 4-disk - Generalisation - Ellipse learned map from imperfect visible to corrected visible and learned invisible.

	MSE	PSNR	SSIM
$\mathcal{NN}_{\text{ResU-Net}}(p_0^{\text{I}_{\text{vis}}})$	$2.0000 \cdot 10^{-4}$	36.9776	0.9398
$\mathcal{NN}_{\text{ResU-Net}}(Q_j^{\text{I}_{\text{vis}}})$	$1.0000 \cdot 10^{-4}$	39.8984	0.9446
$\mathcal{NN}_{\text{ResCor}}(Q_j^{\text{I}_{\text{vis}}})$	$2.9599 \cdot 10^{-5}$	45.2885	0.96866

7. Realistic Data. In this section we evaluate performance of our method on an *in-vivo* vessel data set. Our data set of vessel images is generated by randomly cropping images from the DRIVE data set for retinal vessel segmentation¹⁰. The re-sampled to 192×96 and normalised to $[0,1]$ vessel images constitute the top half of the test image, with bottom half all 0, resulting in test images of size 192×192 , see [Figure 14](#). We assume homogeneous speed of

¹⁰<https://drive.grand-challenge.org/>

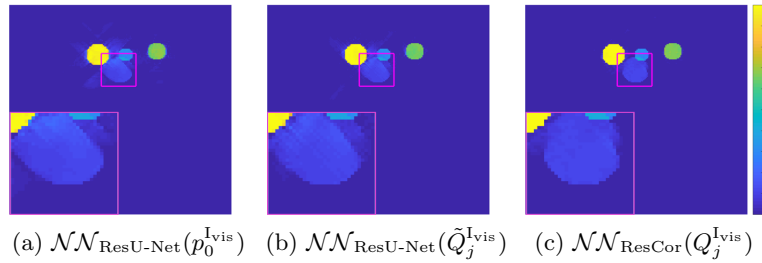


Figure 13: 4-disk Generalisation - Visualisation of generalisation performance of correcting the visible and learning the invisible from ellipse data to 4-disk phantom ($\theta_{\max} = \pi/4$): (a-c) different learned reconstructions.

sound $c = 1500\text{m/s}$. The pressure time series is recorded every $h_t = 66.67\text{ns}$ by a line sensor, placed on top of the domain, with image matching resolution, *i.e.* $h_{\mathbf{x}} = 10\mu\text{m}$ resulting in a 272×192 PAT data volume. The sensitivity angle $\theta_{\max} = 2\pi/9$ is slightly smaller (and so is the visibility cone) than in the previous examples. 2000 images are used for training, 200 images for validation and 200 for testing.

We perform the visible reconstruction (**VR**) in fully wedge restricted Curvelet frame with 3 scales and 12 angles (at the 2nd coarse scale) with regularisation parameter $\tau = 1 \cdot 10^{-4}$ and 50 iterations. As we are in the imperfect learning scenario, we train a matching ResCorNet with loss (**IPL**) and weights $\alpha_F = 2$, $\alpha_{SF} = 2$ and $\alpha_C = 1$ in the same regime as outlined in section 6.

The Coronae coefficient based learning $\mathcal{NN}_{\text{ResU-Net}}(\tilde{Q}_j^{\text{Ivis}})$ and $\mathcal{NN}_{\text{ResCor}}(Q_j^{\text{Ivis}})$ outperforms image based learning $\mathcal{NN}_{\text{ResU-Net}}(p_0^{\text{Ivis}})$ as clearly visible in reconstructions in Figure 14. $\mathcal{NN}_{\text{ResU-Net}}(p_0^{\text{Ivis}})$ suffers from strong limited-view artefacts while $p_0^{\text{Ivis}}_{\text{TV}+}$ fails to recover the invisible vessel edges completely. Zooming in Figure 14 (red and green insets) corroborates that ResCorNet produces smooth background, sharp and detailed vessel edges and well matched contrasts. Some of these are also present in the other reconstructions but ResCorNet is unique in achieving all these goals simultaneously. This is reminiscent of ResCorNet performance for the ellipse data set (see subsection 6.3).

The quantitative analysis is summarised in Table 5. Most notably, we observe a large performance leap across all the measures between the methods learning Coronae coefficients and those learning images which reaffirms the benefits of Coronae representation in this context.

8. Conclusion. The paper rigorously builds a framework where images are nearly optimally represented in a fully wedge restricted Curvelet frame allowing splitting into visible/invisible components, which are optimally matched with the range/null space of the forward operator. All computations can be performed efficiently in Fourier domain. The network architecture is carefully designed to match both the visible/invisible split and the multiscale decomposition induced by the frame working with Coronae coefficients of the visible and invisible image components. Even sole learning of Coronae coefficients results in a substantial improvement on an image based learned post-processing using standard U-Net. The resulting

Table 5: Vessels - Map from imperfect visible to corrected visible and learned invisible. Imaging metrics averaged over test set. Note, in the top two rows perfect visible component $p_0^{\text{P}_{\text{vis}}}$ is used as a ground truth while in the remaining rows we use the original image p_0 .

	MSE	PSNR	SSIM
p_0^{Linear}	$1.3135 \cdot 10^{-3} \pm 5.0308 \cdot 10^{-4}$	29.1241 ± 1.6788	0.8836 ± 0.0529
$p_0^{\ell_1^{\text{vis}}}$	$2.5338 \cdot 10^{-4} \pm 1.4832 \cdot 10^{-4}$	36.5491 ± 2.2176	0.9537 ± 0.0330
$p_0^{\ell_1^{\text{vis}}}$	$1.0201 \cdot 10^{-2} \pm 6.6000 \cdot 10^{-3}$	20.7758 ± 2.8440	0.7947 ± 0.1086
$p_0^{\text{TV}+}$	$4.3110 \cdot 10^{-3} \pm 3.0828 \cdot 10^{-3}$	24.7764 ± 3.3682	0.9398 ± 0.0292
$\mathcal{NN}_{\text{ResU-Net}}(p_0^{\text{vis}})$	$4.5594 \cdot 10^{-2} \pm 1.7357 \cdot 10^{-2}$	13.7066 ± 1.6040	0.6562 ± 0.1104
$\mathcal{NN}_{\text{ResU-Net}}(\tilde{Q}_j^{\text{vis}})$	$7.4186 \cdot 10^{-4} \pm 6.6170 \cdot 10^{-4}$	32.3976 ± 2.9230	0.9540 ± 0.0717
$\mathcal{NN}_{\text{ResCor}}(Q_j^{\text{vis}})$	$7.5803 \cdot 10^{-4} \pm 7.0400 \cdot 10^{-4}$	32.4036 ± 3.0706	0.9611 ± 0.0714

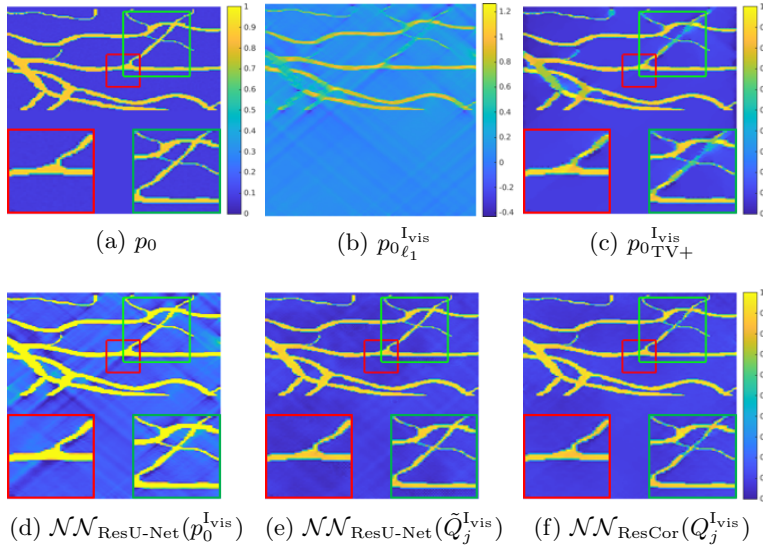


Figure 14: Vessels - Visualisation of the results for correcting the visible and learning the invisible on one test image ($\theta_{\max} = 2\pi/9$): (a) the initial pressure p_0 (ground truth), (b) the imperfect visible component reconstruction via **(VR)**, (c) total variation regularised solution with non-negativity constraint, (d-f) different learned reconstructions.

scheme implementing the reconstructing the visible and learning the invisible strategy decouples the forward model from the training process at no detriment to reconstruction accuracy, which results in a stark performance benefit and a better interpretability compared to model based learning which is considered the gold standard (at least in terms of image quality) among learned reconstructions.

We believe that our framework for this particular class of limited-view problems in photoacoustic tomography will further interest in applying similar ideas to other inverse problems, in particular application to limited-angle parallel CT is immediate. As with all learned methods, performance of our methods strongly depends on appropriateness and quality of the training

data. Finally, we note that extension of our method to 3D is conceptually straightforward and, as no expensive forward/adjoint operators are evaluated in training, it is computationally feasible.

Appendix A. Adjoint PAT Fourier Operator. By definition, the adjoint PAT Fourier operator ($\hat{\mathbf{A}}^*$) satisfies the equality

$$(A.1) \quad \langle \hat{g}, \hat{\mathbf{A}}\hat{p}_0 \rangle = \langle \hat{\mathbf{A}}^* g, \hat{p}_0 \rangle$$

for any real and even w.r.t. first variable functions $\hat{g}(\omega/c, \mathbf{k}_S)$, $\hat{p}(\omega/c, \mathbf{k}_S)$, $(\omega/c, \mathbf{k}_S) \in \mathcal{R}_{\mathbf{A}} \subset \mathbb{R}^d$ and $\hat{p}_0(\mathbf{k}_\perp, \mathbf{k}_S)$, $(\mathbf{k}_\perp, \mathbf{k}_S) \in \mathbb{R}^d$ with sufficient regularity and decay (essentially in Schwarz space over \mathbb{R}^d) so that all the operations are well defined and $\langle \cdot, \cdot \rangle$ is the standard L_2 scalar product which we restrict to $\mathcal{R}_{\mathbf{A}}$ for functions over $(\omega/c, \mathbf{k}_S) \in \mathcal{R}_{\mathbf{A}}$.

Substituting the action of the forward operator $\hat{\mathbf{A}}$ on \hat{p}_0 , $\hat{p}(\omega/c, \mathbf{k}_S) = \hat{\mathbf{A}}\hat{p}_0(\mathbf{k}_\perp, \mathbf{k}_S)$, on the left hand side of (A.1), we obtain

$$(A.2) \quad \begin{aligned} \langle \hat{g}, \hat{\mathbf{A}}\hat{p}_0 \rangle &= \langle \hat{g}(\omega/c, \mathbf{k}_S), \hat{p}(\omega/c, \mathbf{k}_S) \rangle \\ &= 2 \int_{\mathbb{R}_0} \int_{\mathbb{R}^{d-1}} \hat{g}(\omega/c, \mathbf{k}_S) \frac{\omega/c}{\sqrt{(\omega/c)^2 - |\mathbf{k}_S|^2}} \hat{p}_0 \left(\sqrt{(\omega/c)^2 - |\mathbf{k}_S|^2}, \mathbf{k}_S \right) d(\omega/c) d\mathbf{k}_S \end{aligned}$$

where we used the even symmetry in the first variable of $\hat{g}(\omega/c, \mathbf{k}_S)$, $\hat{p}(\omega/c, \mathbf{k}_S)$, which in turn implies even symmetry of $\hat{p}_0(\mathbf{k}_\perp, \mathbf{k}_S)$ (used later), to restrict the the first integral to non-negative real axis \mathbb{R}_0 .

In the next step we make use of change of variables induced by the dispersion relation in the wave equation (3.3), $(\mathbf{k}_\perp, \mathbf{k}_S) \leftarrow \left(\sqrt{(\omega/c)^2 - |\mathbf{k}_S|^2}, \mathbf{k}_S \right)$, $\mathbf{k}_\perp \geq 0$, assumed continued with even symmetry for $\mathbf{k}_\perp < 0$. The Jacobian of the change of coordinates yields

$$d\mathbf{k}_\perp = \frac{\omega/c}{\sqrt{(\omega/c)^2 - |\mathbf{k}_S|^2}} d(\omega/c).$$

Executing the change of coordinates in the last line of (A.2), the factor gets absorbed into the volume element and we are left with

$$\begin{aligned} \langle \hat{g}, \hat{\mathbf{A}}\hat{p}_0 \rangle &= \iint_{\mathbb{R}^d} \hat{g}(|\mathbf{k}|, \mathbf{k}_S) \hat{p}_0(\mathbf{k}_\perp, \mathbf{k}_S) d\mathbf{k}_\perp d\mathbf{k}_S \\ &= \langle \hat{g}(|\mathbf{k}|, \mathbf{k}_S), \hat{p}_0(\mathbf{k}_\perp, \mathbf{k}_S) \rangle, \end{aligned}$$

where the factor 2 is accounted for by extension of the integration of the product of even functions from \mathbb{R}_0 back to \mathbb{R} . Comparing the above equation to the right hand side of defining equality (A.1), we immediately read out the action of the adjoint operator on $\hat{g}(\omega/c, \mathbf{k}_S)$ as

$$(A.3) \quad \hat{\mathbf{A}}^* \hat{g}(\omega/c, \mathbf{k}_S) = \hat{g}(|\mathbf{k}|, \mathbf{k}_S).$$

REFERENCES

[1] J. ADLER AND O. ÖKTEM, *Solving ill-posed inverse problems using iterative deep neural networks*, Inverse Problems, 33 (2017), p. 124007.

[2] J. ADLER AND O. ÖKTEM, *Learned primal-dual reconstruction*, IEEE transactions on medical imaging, 37 (2018), pp. 1322–1332.

[3] H. ANDRADE-LOARCA, G. KUTYNIOK, O. ÖKTEM, AND P. PETERSEN, *Deep microlocal reconstruction for limited-angle tomography*, arXiv preprint arXiv:2108.05732, (2021).

[4] H. ANDRADE-LOARCA, G. KUTYNIOK, O. ÖKTEM, AND P. C. PETERSEN, *Extraction of digital wavefront sets using applied harmonic analysis and deep neural networks*, SIAM Journal on Imaging Sciences, 12 (2019), pp. 1936–1966.

[5] S. ANTHOLZER, M. HALTMEIER, R. NUSTER, AND J. SCHWAB, *Photoacoustic image reconstruction via deep learning*, in Photons Plus Ultrasound: Imaging and Sensing 2018, vol. 10494, International Society for Optics and Photonics, 2018, p. 104944U.

[6] S. ANTHOLZER, M. HALTMEIER, AND J. SCHWAB, *Deep learning for photoacoustic tomography from sparse data*, Inverse problems in science and engineering, 27 (2019), pp. 987–1005.

[7] S. ANTHOLZER, J. SCHWAB, AND M. HALTMEIER, *Deep learning versus ℓ_1 -minimization for compressed sensing photoacoustic tomography*, in 2018 IEEE International Ultrasonics Symposium (IUS), IEEE, 2018, pp. 206–212.

[8] S. ARRIDGE, P. BEARD, M. BETCKE, B. COX, N. HUYNH, F. LUCKA, O. OGUNLADE, AND E. ZHANG, *Accelerated high-resolution photoacoustic tomography via compressed sensing*, Physics in Medicine & Biology, 61 (2016), p. 8908.

[9] S. ARRIDGE, P. MAASS, O. ÖKTEM, AND C.-B. SCHÖNLIEB, *Solving inverse problems using data-driven models*, Acta Numerica, 28 (2019), pp. 1–174.

[10] S. R. ARRIDGE, M. M. BETCKE, B. T. COX, F. LUCKA, AND B. E. TREEBY, *On the adjoint operator in photoacoustic tomography*, Inverse Problems, 32 (2016), p. 115012.

[11] P. BEARD, *Biomedical photoacoustic imaging*, Interface focus, 1 (2011), pp. 602–631.

[12] A. BECK AND M. TEBOULLE, *A fast iterative shrinkage-thresholding algorithm for linear inverse problems*, SIAM journal on imaging sciences, 2 (2009), pp. 183–202.

[13] M. M. BETCKE, B. T. COX, N. HUYNH, E. Z. ZHANG, P. C. BEARD, AND S. R. ARRIDGE, *Acoustic wave field reconstruction from compressed measurements with application in photoacoustic tomography*, IEEE Transactions on Computational Imaging, 3 (2017), pp. 710–721.

[14] Y. E. BOINK, C. BRUNE, AND S. MANOHAR, *Robustness of a partially learned photoacoustic reconstruction algorithm*, in Photons Plus Ultrasound: Imaging and Sensing 2019, vol. 10878, International Society for Optics and Photonics, 2019, p. 108781D.

[15] Y. E. BOINK, M. J. LAGERWERF, W. STEENBERGEN, S. A. VAN GILS, S. MANOHAR, AND C. BRUNE, *A reconstruction framework for total generalised variation in photoacoustic tomography*, ArXiv e-prints, (2017).

[16] Y. E. BOINK, S. MANOHAR, AND C. BRUNE, *A partially-learned algorithm for joint photo-acoustic reconstruction and segmentation*, IEEE transactions on medical imaging, 39 (2019), pp. 129–139.

[17] Y. E. BOINK, S. A. VAN GILS, S. MANOHAR, AND C. BRUNE, *Sensitivity of a partially learned model-based reconstruction algorithm*, PAMM, 18 (2018), p. e201800222.

[18] T. A. BUBBA, M. GALINIER, M. LASSAS, M. PRATO, L. RATTI, AND S. SILTANEN, *Deep neural networks for inverse problems with pseudodifferential operators: an application to limited-angle tomography*, SIAM Journal on Imaging Sciences, (2021).

[19] T. A. BUBBA, G. KUTYNIOK, M. LASSAS, M. MÄRZ, W. SAMEK, S. SILTANEN, AND V. SRINIVASAN, *Learning the invisible: A hybrid deep learning-shearlet framework for limited angle computed tomography*, Inverse Problems, 35 (2019), p. 064002.

[20] E. CANDES, L. DEMANET, D. DONOHO, AND L. YING, *Fast discrete curvelet transforms*, multiscale modeling & simulation, 5 (2006), pp. 861–899.

[21] E. J. CANDES AND L. DEMANET, *The curvelet representation of wave propagators is optimally sparse*, Communications on Pure and Applied Mathematics, 58 (2005), pp. 1472–1528.

[22] E. J. CANDÈS AND D. L. DONOHO, *New tight frames of curvelets and optimal representations of objects with piecewise $c2$ singularities*, Communications on Pure and Applied Mathematics: A Journal Issued by the Courant Institute of Mathematical Sciences, 57 (2004), pp. 219–266.

[23] B. T. COX AND P. C. BEARD, *Fast calculation of pulsed photoacoustic fields in fluids using k -space*

methods, The Journal of the Acoustical Society of America, 117 (2005), pp. 3616–3627.

[24] D. L. DONOHO, *Sparse components of images and optimal atomic decompositions*, Constructive Approximation, 17 (2001), pp. 353–382.

[25] D. FINCH AND S. K. PATCH, *Determining a function from its mean values over a family of spheres*, SIAM journal on mathematical analysis, 35 (2004), pp. 1213–1240.

[26] J. FRIKEL, *A new framework for sparse regularization in limited angle x-ray tomography*, in 2010 IEEE International Symposium on Biomedical Imaging: From Nano to Macro, 2010, pp. 824–827, <https://doi.org/10.1109/ISBI.2010.5490113>.

[27] J. FRIKEL, *Sparse regularization in limited angle tomography*, Applied and Computational Harmonic Analysis, 34 (2013), pp. 117–141.

[28] J. FRIKEL AND M. HALTMEIER, *Efficient regularization with wavelet sparsity constraints in photoacoustic tomography*, Inverse Problems, 34 (2018), p. 024006, <https://doi.org/10.1088/1361-6420/aaa0ac>, <https://doi.org/10.1088/1361-6420/aaa0ac>.

[29] J. FRIKEL AND E. T. QUINTO, *Characterization and reduction of artifacts in limited angle tomography*, Inverse Problems, 29 (2013), p. 125007, <https://doi.org/10.1088/0266-5611/29/12/125007>, <https://doi.org/10.1088/0266-5611/29/12/125007>.

[30] J. FRIKEL AND E. T. QUINTO, *Artifacts in incomplete data tomography with applications to photoacoustic tomography and sonar*, SIAM Journal on Applied Mathematics, 75 (2015), pp. 703–725, <http://www.jstor.org/stable/24511467>.

[31] X. GLOROT AND Y. BENGIO, *Understanding the difficulty of training deep feedforward neural networks*, in Proceedings of the thirteenth international conference on artificial intelligence and statistics, JMLR Workshop and Conference Proceedings, 2010, pp. 249–256.

[32] S. GUAN, A. A. KHAN, S. SIKDAR, AND P. V. CHITNIS, *Fully dense unet for 2-d sparse photoacoustic tomography artifact removal*, IEEE journal of biomedical and health informatics, 24 (2019), pp. 568–576.

[33] M. HALTMEIER, T. BERER, S. MOON, AND P. BURGHOLZER, *Compressed sensing and sparsity in photoacoustic tomography*, Journal of Optics, 18 (2016), p. 114004.

[34] K. HAMMERNIK, T. KLATZER, E. KOBLER, M. P. RECHT, D. K. SODICKSON, T. POCK, AND F. KNOLL, *Learning a variational network for reconstruction of accelerated mri data*, Magnetic resonance in medicine, 79 (2018), pp. 3055–3071.

[35] A. HAUPTMANN, B. COX, F. LUCKA, N. HUYNH, M. BETCKE, P. BEARD, AND S. ARRIDGE, *Approximate k-space models and deep learning for fast photoacoustic reconstruction*, in International Workshop on Machine Learning for Medical Image Reconstruction, Springer, 2018, pp. 103–111.

[36] A. HAUPTMANN AND B. T. COX, *Deep learning in photoacoustic tomography: Current approaches and future directions*, Journal of Biomedical Optics, 25 (2020), p. 112903.

[37] A. HAUPTMANN, F. LUCKA, M. BETCKE, N. HUYNH, J. ADLER, B. COX, P. BEARD, S. OURSELIN, AND S. ARRIDGE, *Model-based learning for accelerated, limited-view 3-d photoacoustic tomography*, IEEE transactions on medical imaging, 37 (2018), pp. 1382–1393.

[38] C. HUANG, K. WANG, L. NIE, L. V. WANG, AND M. A. ANASTASIO, *Full-wave iterative image reconstruction in photoacoustic tomography with acoustically inhomogeneous media*, IEEE transactions on medical imaging, 32 (2013), pp. 1097–1110.

[39] N. HUYNH, F. LUCKA, E. ZHANG, M. BETCKE, S. ARRIDGE, P. BEARD, AND B. COX, *Sub-sampled fabry-perot photoacoustic scanner for fast 3d imaging*, in Photons Plus Ultrasound: Imaging and Sensing 2017, vol. 10064, International Society for Optics and Photonics, 2017, p. 100641Y.

[40] K. H. JIN, M. T. MCCANN, E. FROUSTEY, AND M. UNSER, *Deep convolutional neural network for inverse problems in imaging*, IEEE Transactions on Image Processing, 26 (2017), pp. 4509–4522.

[41] E. KANG, J. MIN, AND J. C. YE, *A deep convolutional neural network using directional wavelets for low-dose x-ray ct reconstruction*, Medical physics, 44 (2017), pp. e360–e375.

[42] K. P. KÖSTLI, M. FRENZ, H. BEBIE, AND H. P. WEBER, *Temporal backward projection of optoacoustic pressure transients using fourier transform methods*, Physics in Medicine & Biology, 46 (2001), p. 1863.

[43] H. LAN, D. JIANG, C. YANG, AND F. GAO, *Y-net: a hybrid deep learning reconstruction framework for photoacoustic imaging in vivo*, arXiv preprint arXiv:1908.00975, (2019).

[44] L. NIE AND X. CHEN, *Structural and functional photoacoustic molecular tomography aided by emerging contrast agents*, Chemical Society Reviews, 43 (2014), pp. 7132–7170.

[45] B. PAN, M. BETCKE, S. ARRIDGE, F. LUCKA, B. COX, N. HUYNH, P. BEARD, AND E. ZHANG, *Photoacoustic reconstruction using sparsity in curvelet frame: Image versus data domain*, IEEE Transactions on Computational Imaging, (2021).

[46] J. QIAN, P. STEFANOV, G. UHLMANN, AND H. ZHAO, *An efficient neumann series-based algorithm for thermoacoustic and photoacoustic tomography with variable sound speed*, SIAM Journal on Imaging Sciences, 4 (2011), pp. 850–883.

[47] E. T. QUINTO, *Singularities of the x-ray transform and limited data tomography in \mathbb{R}^2 and \mathbb{R}^3* , SIAM Journal on Mathematical Analysis, 24 (1993), pp. 1215–1225.

[48] E. T. QUINTO, *Artifacts and visible singularities in limited data x-ray tomography*, Sensing and Imaging, 18 (2017), p. 9.

[49] J. SCHWAB, S. ANTHOLZER, AND M. HALTMEIER, *Deep null space learning for inverse problems: convergence analysis and rates*, Inverse Problems, 35 (2019), p. 025008.

[50] J. SCHWAB, S. ANTHOLZER, AND M. HALTMEIER, *Learned backprojection for sparse and limited view photoacoustic tomography*, in Photons Plus Ultrasound: Imaging and Sensing 2019, vol. 10878, International Society for Optics and Photonics, 2019, p. 1087837.

[51] J. SCHWAB, S. ANTHOLZER, R. NUSTER, AND M. HALTMEIER, *Real-time photoacoustic projection imaging using deep learning*, arXiv preprint arXiv:1801.06693, (2018).

[52] J. SCHWAB, S. PEREVERZYEV JR, AND M. HALTMEIER, *A galerkin least squares approach for photoacoustic tomography*, SIAM Journal on Numerical Analysis, 56 (2018), pp. 160–184.

[53] H. SHAN, G. WANG, AND Y. YANG, *Accelerated correction of reflection artifacts by deep neural networks in photo-acoustic tomography*, Applied Sciences, 9 (2019), p. 2615.

[54] H. SHAN, C. WIEDEMAN, G. WANG, AND Y. YANG, *Simultaneous reconstruction of the initial pressure and sound speed in photoacoustic tomography using a deep-learning approach*, in Novel Optical Systems, Methods, and Applications XXII, vol. 11105, International Society for Optics and Photonics, 2019, p. 1110504.

[55] J.-L. STARCK, E. J. CANDÈS, AND D. L. DONOHO, *The curvelet transform for image denoising*, IEEE Transactions on Image Processing, 11 (2002), pp. 670–684.

[56] P. STEFANOV AND G. UHLMANN, *Thermoacoustic tomography with variable sound speed*, Inverse Problems, 25 (2009), p. 075011.

[57] K. S. VALLURU, K. E. WILSON, AND J. K. WILLMANN, *Photoacoustic imaging in oncology: translational preclinical and early clinical experience*, Radiology, 280 (2016), pp. 332–349.

[58] K. WANG AND M. A. ANASTASIO, *Photoacoustic and thermoacoustic tomography: image formation principles*, in Handbook of Mathematical Methods in Imaging, Springer, 2011, pp. 781–815.

[59] L. V. WANG, *Multiscale photoacoustic microscopy and computed tomography*, Nature photonics, 3 (2009), pp. 503–509.

[60] J. XIA AND L. V. WANG, *Small-animal whole-body photoacoustic tomography: a review*, IEEE Transactions on Biomedical Engineering, 61 (2013), pp. 1380–1389.

[61] M. XU AND L. V. WANG, *Universal back-projection algorithm for photoacoustic computed tomography*, Physical Review E, 71 (2005), p. 016706.

[62] Y. XU, D. FENG, AND L. V. WANG, *Exact frequency-domain reconstruction for thermoacoustic tomography. i. planar geometry*, IEEE transactions on medical imaging, 21 (2002), pp. 823–828.

[63] Y. XU, L. V. WANG, G. AMBARTSOUMIAN, AND P. KUCHMENT, *Reconstructions in limited-view thermoacoustic tomography*, Medical physics, 31 (2004), pp. 724–733.

[64] C. YANG, H. LAN, AND F. GAO, *Accelerated photoacoustic tomography reconstruction via recurrent inference machines*, in 2019 41st Annual International Conference of the IEEE Engineering in Medicine and Biology Society (EMBC), IEEE, 2019, pp. 6371–6374.

[65] Y. ZHOU, J. YAO, AND L. V. WANG, *Tutorial on photoacoustic tomography*, Journal of biomedical optics, 21 (2016), p. 061007.

[66] B. ZHU, J. Z. LIU, S. F. CAULEY, B. R. ROSEN, AND M. S. ROSEN, *Image reconstruction by domain-transform manifold learning*, Nature, 555 (2018), pp. 487–492.